

1 Title: Sediment accumulation and paleoceanography of the northeastern Caribbean: IODP Site U1396 off
2 Montserrat, Lesser Antilles

3 Author Names and affiliations:

4 Andrew J. Fraass¹, Deborah Wall-Palmer^b, R. Mark Leckie^a, Robert G. Hatfield^c, Stephen J. Burns^a, Anne
5 Le Friant^d, Osamu Ishizuka^e, Mohammed Aljahdali^h, Martin Jutzelerⁱ, Michael Martínez-Colón^j, Martin
6 Palmer^k, Peter J. Talling^k

7
8 ^a University of Massachusetts, Dept. of Geosciences, 233 Morrill Science Center, 611 N. Pleasant St.,
9 Amherst, MA 01003, USA

10 ^b Plymouth University, School of Geography, Earth, and Environmental Sciences, Plymouth, UK

11 ^c College of Earth, Ocean, and Atmospheric Sciences, 104 CEOAS Admin Building, Oregon State
12 University, Corvallis, OR 97331, USA

13 ^d Institut de Physique du Globe de Paris, Sorbonne Paris Cité and CNRS UMR 7154, Paris, France

14 ^e Geological Survey of Japan (AIST), Ibaraki, Japan

15 ^h Department of Earth, Ocean and Atmospheric Sciences, Florida State University,
16 108 Carraway Building, Tallahassee FL 32306-0001

17 ⁱ School of Physical Sciences and Centre of Excellence in Ore Deposits (CODES),
18 University of Tasmania, Hobart TAS 7001 Australia.

19 ^j College of Marine Science, University of South Florida, St. Petersburg, 140 7th
20 Avenue South, St. Petersburg FL 33701, USA

21 ^k School of Ocean and Earth Science, National Oceanography Centre, University of
22 Southampton, European Way, Southampton SO14 3ZH, UK

23

24 ¹ Present Address: Department of Paleobiology, National Museum of Natural History, Smithsonian
25 Institution, Washington, Dist. of Columbia, USA

26 Corresponding Author: Andrew J. Fraass (FraassA@si.edu)

27

28

29 **Abstract**

30 Site U1396 was piston cored as a part of Integrated Ocean Drilling Project Expedition 340 to
31 establish a long record for Lesser Antilles volcanism. A ~150 m sediment succession was
32 recovered from three holes on a bathymetric high ~33 km southwest of Montserrat. A series of
33 shipboard and newly-generated chronostratigraphic tools (biostratigraphy,
34 magnetostratigraphy, astrochronology, and stable isotope chemostratigraphy) were employed
35 to generate an integrated age model. Two possible chronostratigraphic interpretations for the
36 Brunhes chron are presented, with hypotheses to explain the discrepancies seen between this
37 study and Wall-Palmer et al. (2014). The recent Wade et al. (2011) planktic foraminiferal
38 biostratigraphic calibration is tested, revealing good agreement between primary datums
39 observed at Site U1396 and calibrated ages, but significant mismatches for some secondary
40 datums. Sedimentation rates are calculated, both including and excluding the contribution of
41 discrete volcanic sediment layers within the succession. Rates are found to be 'pulsed' or highly
42 variable within the Pliocene interval, declining through the 1.5-2.4 Ma interval, and then lower
43 through the Pleistocene. Different explanations for the trends in the sedimentation rates are
44 discussed, including orbitally-forced biogenic production spikes, elevated contributions of
45 cryptotephra (dispersed ash), and changes in bottom water sourcing and flow rates with
46 increased winnowing in the area of Site U1396 into the Pleistocene.

47

48

49 **INTRODUCTION**

50 Montserrat Island is part of the Lesser Antilles island arc in the Caribbean Sea. The
51 Lesser Antilles arc has a volcanic history dating back to the mid-Oligocene, though the western
52 arc has been active since the early Miocene (Macdonald et al., 2000). Montserrat is one of the
53 youngest islands in the arc and was subaerially built over three major volcanic centers, the
54 oldest deposit dated to ~2,600 ka (Harford et al., 2002). The current phase of volcanism began in
55 1995 and at South Soufrière Hills has produced numerous volcanic deposits that range from
56 pyroclastic material deposited on land and in the surrounding ocean, to substantial marine
57 debris flows mapped using bathymetric surveys (Le Friant et al., 2010; Crutchley et al., 2013).
58 Because ~65% of volcanoclastic material is transported into the ocean after an eruption (Le
59 Friant et al., 2010), it is critical to establish a robust geologic record from detailed offshore data.

60 The history of Montserrat volcanism has been largely extended by the use of offshore
61 sediments, and is an area of active research (e.g., Cassidy et al., 2013, 2014; Le Friant et al., 2008,
62 2010; Trofimovs et al., 2010; Shipboard Scientific Party, 2012; Wall-Palmer et al., 2014; McCanta
63 et al., 2015). This history also has relevance to the hazards posed by volcanic activity to the
64 surrounding communities. Landslides, in particular, may be a source of concern as potential
65 tsunamogenic events, because they emplace substantial amounts of material ($>380 \times 10^6 \text{ m}^3$)
66 into the ocean in a short period of time, as seen both in the modern (e.g., Herd et al., 2006) and
67 geological record (~14 ka; Trofimovs et al., 2010). Although some landslides and debris
68 avalanches have been associated with the recent activity of the Soufrière Hills volcano (e.g.,
69 Herd et al., 2006), landslides identified in the geological record have less certain affinities and
70 may be related to rapid sea-level rise associated with transitioning from glacial to interglacial
71 conditions (Trofimovs et al., 2010; Coussens et al., 2016). Understanding the past history of

72 volcanic activity in the Lesser Antilles, and the frequency and cause of previous landslides, is
73 therefore important for the prediction of future potential geohazards. With that in mind,
74 Integrated Ocean Drilling Program (IODP) Expedition 340 cored three sites to examine the
75 structure, composition, and history of the sediments surrounding Montserrat. Here, we discuss
76 hemipelagic sedimentation from U1396, a coring site situated on a topographic high with low
77 sedimentation rates, and where erosion is likely minimal.

78 During the Pliocene and Pleistocene, the Caribbean Sea is sensitive to the presence or
79 absence of the Panamanian Isthmus, separating the Atlantic and Pacific oceans (e.g., Groeneveld
80 et al., 2014). Precise timing and the oceanographic impacts of the Panamanian Isthmus closure
81 remains a controversial issue that has yet to be resolved (see discussion in Molnar, 2008). Some
82 authors suggest that the closure increased meridional overturning circulation (e.g., Keigwin,
83 1982; Haug and Tiedemann, 1998; Osborne et al., 2014) while others suggest, for instance, a
84 profound shift to oligotrophic waters (e.g., Chaisson, 2003; Jain and Collins, 2007). Although
85 these hypotheses could be interrelated, their studies suggest differences in timing, with
86 differences greater than a million years.

87 Biostratigraphy is inherently imprecise. As all of the data are biological, they are thus
88 filtered through various ‘noisy’ processes. Planktic foraminifera, for example, are prone to
89 ecological and climatological fluctuations, and regional distributions controlled by
90 oceanographic processes (Bé & Tolderlund, 1971), all of which can affect the stratigraphic level
91 of highest and lowest appearances. Taphonomic processes, such as winnowing or differential
92 preservation, for example, can also change the true ‘Top’ or ‘Bottom’ of a species. Despite
93 inherent difficulties, the utility and value of planktic foraminiferal biostratigraphy is well-

94 established. Most biostratigraphic calibrations use meridional zonation schemes, divided into
95 'tropical' or 'tropical-subtropical' zonation schemes, while additional subdivisions (Atlantic vs.
96 Pacific Ocean calibrations) alleviate some of the regional differences. The recent Wade et al.
97 (2011) calibration refined existing datums from Berggren and Pearson (2006; and references
98 therein) and established a number of new datums. Wade et al. (2011) also used the Cande and
99 Kent (1995) geomagnetic polarity timescale, as well as more recent astrochronologically-
100 calibrated timescales (Pälike et al., 2006; Lourens et al., 2004) to produce robust datum ages.
101 However, while these dates are robust at a single site or regionally, it is not commonplace to
102 define an 'error' for the datums. Biostratigraphic originations, even in rapidly spreading
103 species, are at best only geologically instantaneous, as a species cannot arise simultaneously
104 around the globe. Similarly, true biological extinctions are likely a series of regional extinctions
105 that finally culminate in the complete elimination of the entire species. One reason that planktic
106 foraminifera persist as a premier biostratigraphic system is due to their wide, and largely
107 homogenous, biogeographic ranges (Bé & Tolderlund, 1971). Thus, their 'regional' originations
108 and extinctions occur at the scale of tropical-subtropical subdivisions.

109 IODP Site U1396 (Figure 1) presents an ideal locality to verify the last 4.5 myr of the
110 Wade calibration. Shipboard analysis suggests that the sediments from Site U1396 represent
111 relatively continuous sedimentation and an excellent paleomagnetic stratigraphy was recovered
112 (Expedition 340 Scientists, 2013). Shipboard planktic foraminiferal and nannofossil
113 biostratigraphic analyses determined that all primary datum species, and the majority of the
114 secondary datum species, were present at the site. Detailed shipboard core descriptions
115 established five main units (A-E). Unit A is represented by approximately 40 cm of bioclastic

116 sand near the sediment water interface. Unit B is a ~110-m thick sequence of hemipelagic mud
117 interrupted by layers of tephra. Unit C is likely an artifact coring, 'flow-in' from a pumice layer
118 resulting an abnormal stratigraphy. Unit D is a volcanic breccia, whereas Unit E is similar to
119 Unit B (Expedition 340 Scientists, 2013). Units B and E constitute the vast majority of
120 sedimentation at this site.

121 The aim of this study is twofold. The first aim is to produce a robust age-model at or
122 near the marine isotope stage resolution. Although the recovered sediments cannot address
123 early aspects of the Panamanian Isthmus closure history, which occurred in the Miocene
124 (Keigwin, 1982; Haug and Tiedemann, 1998), it can address questions about the final closure
125 (~3-4 Ma) and the impacts on the biota, productivity, and circulation with the Caribbean Sea
126 (e.g., Jain and Collins, 2007). The ~150 m cored deposits at Site U1396 represent 4.5 myr of
127 sedimentation. We built a robust age-model to address these questions.

128 Second, this site presents a good opportunity to test the newly-established datums from
129 Wade et al. (2013). To those ends, several chronostratigraphic tools were employed.
130 Astrochronological tuning was performed on the color reflectance parameter L* (Brightness)
131 from shipboard physical properties data using the 'astrochron' package within the R
132 programming environment (Meyers, 2014; R Core Team, 2015). A ~9-kyr resolution benthic
133 foraminiferal $\delta^{18}\text{O}$ record was generated and compared to the LR04 benthic foraminifera stack
134 (Lisiecki & Raymo, 2005). Planktic foraminiferal biostratigraphy was also carried out at the
135 same resolution (~9 kyr), to provide support for the other chronostratigraphic techniques and to
136 be checked against the calibrations.

137

138 **REGIONAL SETTING AND SHIPBOARD RESULTS**

139 Site U1396 is located at 16°30.49'N, 62°27.10'W at ~800 m water depth. It is roughly
140 southwest from the island of Montserrat sitting atop a bathymetric high. Coring at this site was
141 hypothesized to limit the occurrence of turbidites, allowing for a more continuous record of
142 volcanism than possible in other areas offshore of Montserrat. In addition, the sedimentation
143 rates determined for the nearby CARMON-2 site (Le Friant et al., 2008) suggested it would be
144 possible to extend the existing geologic history to 4-5 Ma (Expedition 340 Scientists, 2013). Three
145 holes were cored at Site U1396 using advanced piston coring. Holes U1396A and U1396C each
146 consist of 15 cores and are continuous over 135 m and 140 m, respectively, whereas Hole B is a
147 single 10 m core taken to replicate 340-U1396A-2H which suffered a shattered liner during
148 coring. Lithostratigraphy between the holes correlates well (see below), excluding a single unit
149 (Unit C) in U1396C, which contained a substantial interval of basal flow-in of pumiceous sand
150 (Jutzeler et al., 2014), which does not occur over the same thickness in U1396A. Shipboard age
151 determination suggested that the base of U1396C was older than U1396A, so U1396C was
152 selected as the main hole for biostratigraphic and stable isotope study.

153

154 **METHODS**

155 **Depth scales and shipboard data**

156 Description of the core, preliminary calcareous nannofossil and planktic foraminiferal
157 biostratigraphy, and physical properties data collection (e.g., color reflectance) were all
158 performed onboard the R/V *JOIDES Resolution* during IODP Expedition 340. The initial
159 shipboard age model and resulting sedimentation rates for the Pliocene (~4 cm/kyr) and

160 Pleistocene (~2 cm/kyr) were determined by the paleomagnetic reversal stratigraphy and
161 supported by nannofossil and planktic foraminiferal biostratigraphy (Expedition 340 Scientists,
162 2013). A composite depth scale (CCSF-A) was generated with a primary splice (CCSF-D)
163 (Hatfield 2015). The CCSF-D record relies heavily on core sections from Hole U1396A, in part
164 because it is the most complete record as two 10 cm whole rounds were consistently taken from
165 each Hole C core shortly after core recovery. A tool was created in the R computing
166 environment (R Core Team, 2015) to place off-splice data and all preexisting and newly-
167 generated data into the CCSF-D scale. Figure 2 depicts the process of splicing the color
168 reflectance data and lithostratigraphic data from the initial CSF depth scale to the CCSF-A
169 depth scale, and finally onto the continuous splice. The L* (brightness) and lithostratigraphy
170 data sets both agree well with the magnetic susceptibility based correlation of Hatfield (2015),
171 indicating the compositing process is robust (Figure 2b). We use the revised assessment of the
172 paleomagnetic reversal record here (Hatfield, 2015) rather than the one generated shipboard.
173 Hatfield (2015) did not correlate Core 340-U1396A-2H into the composite section due to issues
174 with the magnetic susceptibility record of the disturbed core. Using both the core description
175 and core photos of Cores 340-U1396A-2H, U1396C-1H, and U1396C-2H we now place 340-
176 U1396A-2H on the U1396A CCSF-A scale using an offset of 1.71 m using lithostratigraphic
177 correlation.

178

179 **Generation of an 'Event-Free' section**

180 Volcanic sedimentation derived from eruption (syn-eruptive *sensu* Carey and Schneider,
181 2011) is geologically instantaneous. Ash deposits, for example, are frequently darker in color

182 than hemipelagic material, and so impart stochastic noise (from a cycle perspective) to an
183 analysis of the expected cyclic bands of sediment produced by Milankovitch or glacial-
184 interglacial periodicity. Also, hemipelagic material is deposited at a different, quasi-continuous,
185 sedimentation rate than the 'instantaneous' ash deposits. Removal of the discrete volcanic
186 deposit intervals, such as ash beds, should result in a cleaner hemipelagic stratigraphic column,
187 and potentially a series of Milankovic-style frequencies that are less dominated by noise.
188 However, this does not alleviate the issue of dispersed ash, as documented by ODP Leg 165 in
189 the Caribbean (Sigurdsson et al. 1997) and within the upper several meters of U1396C (McCanta
190 et al., 2015). An R function was employed to remove the volcanic sediments from the
191 stratigraphy. The function employs the shipboard core description to identify the various
192 sediment types with a major lithology type of volcanic origin, and then removes their
193 thicknesses from the stratigraphy. It then recalculates the depths for the rest of the stratigraphy
194 as if the volcanic sediments were not there resulting in a CCSF-NV (No Volcanics) scale (Figure
195 2 depicts this process). The CCSF-NV scale allows the comparison of three distinct
196 sedimentation rates: composite (hemipelagic+volcanic), hemipelagic, and volcanic.

197

198 **Astrochronological tuning**

199 Astrochronology is a method of age determination that employs the known frequencies
200 of various astronomical parameters (e.g., obliquity) and some high-resolution dataset, in this
201 case sediment brightness, to derive an age model. Astrochronologically tuning of the
202 sedimentary record from Site U1396 was not done independently of other age diagnostic
203 criteria. Instead, approximately half the paleomagnetic datums were used to generate a

204 hemipelagic sedimentation rate (linear sedimentation rate without the thickness of volcanically-
205 sourced sediments). Astrochronological analysis was then performed using 'astrochron', a
206 package developed for R (Meyers, 2014). Tuning was performed in intervals ~0.5 myr in length.
207 L^* was interpolated to 3-kyr intervals, prior to the evolutive harmonic analysis (EHA). The
208 stratigraphic sequence was padded to approximately double the number of points in the
209 interpolated dataset. The window size for the EHA was 140-kyr with a step of 3-kyr. EHA
210 results (e.g., fig 3) suggest the presence of tunable frequencies, despite the still substantial
211 component of noise.

212 Tuning was performed so that there was as good an agreement between age diagnostic
213 criteria and orbital or glacial-interglacial frequencies as possible, but, as previously noted, the
214 signal is still prone to substantial noise due to data interpretation, core recovery, and
215 sedimentological factors. A slight offset in the splice correlation could result in a missed portion
216 of a cycle at splice points, for example. If the sedimentation rate were 4 cm/kyr, an offset in the
217 splice of 2.5 cm would result in a loss of ~1/4 of the 41-kyr obliquity cycle. This would manifest
218 in the EHA diagram by splitting the observed frequency into two pieces, one higher frequency
219 and one lower, with a gap in the middle (Meyers and Sageman, 2014). It is also possible that
220 removing all volcanoclastic beds is overly cautious; some of those sediments may not be
221 geologically instantaneous and may be from redeposition of volcanic components (post-
222 eruptive *sensu* Carey and Schneider, 2011). The presence of cryptotephra (dispersed ash)
223 changes the L^* value of the sediments away from the predicted orbital or glacial-interglacial
224 pattern, and increases the bed thickness. The wide window (140-kyr) accounts for this increase
225 in noise, but it induces a lag. An example of this effect is the smearing of frequencies around the

226 employed paleomagnetic datums. In Figure 3 the white lines above and below the black anchor
227 datum are where the EHA begins to record a change in sedimentation rate; the smearing is a
228 result of the change from one linear sedimentation rate to the next. The window size was a
229 compromise between accounting for this noise and creating an age model responsive to
230 sedimentation rate changes.

231

232 **Micropaleontologic methods**

233 A total of 596 samples were examined for biostratigraphically-important species. Two
234 different strategies were used for sample choice. Within the upper 7 m of Site U1396, a sample
235 spacing of 5 cm (~0.5-2 kyr) was used (these samples were previously used in Wall-Palmer et
236 al., 2014). Below 7 mbsf a sampling resolution of ~9 kyrs was used, based on the shipboard age
237 model, but excluding volcanic sediments. All samples were checked against the Jutzeler et al.
238 (2016) coring disturbance compilation and were found to be outside of all intervals with coring
239 disturbances. For samples below 7 meters, samples were dried for ~24 hours, then soaked in a
240 mild Sparkleen® solution for 24-72 hours, a step necessary to free foraminifera from
241 surrounding sediment. Sediment was washed over a 63 µm sieve before being dried for ~24
242 hours in a 40-50°C oven. Prior to being inspected, samples were dry-sieved over a 150 µm sieve.
243 All identification was performed at the >150 µm size fraction, following the taxonomy of
244 Kennett & Srinivasan (1983). Ages for the biostratigraphic datums follow the Wade et al. (2011)
245 astrochronological calibration (and references therein).

246 Samples within the upper Pleistocene-Holocene Brunhes chron were inspected for
247 *Globorotalia menardii* and *G. tumida*, as the abundances of those taxa have been shown to

248 fluctuate in response to glacial-interglacial cycles (e.g., Ericson and Wollin, 1968; Kennett and
249 Huddlestun, 1972). This biozonation scheme has been employed globally and locally with
250 success (e.g., Reid et al., 1996). Here it was used to continue the data collection of Wall-Palmer
251 et al. (2014), extending their record of %*G. menardii-tumida* (undifferentiated) to the first
252 geomagnetic reversal (i.e., base of the Brunhes chron). Following the Wall-Palmer et al. (2014)
253 methods, samples were dry-sieved over a 355 μm sieve, then a split to ~ 300 individuals was
254 performed using a microsplitter. Total planktic foraminifera and *G. menardii-tumida* tests were
255 counted.

256 Individual foraminifera from near the top or bottom of their range were imaged on a
257 Carl Zeiss EVO 50 XVP scanning electron microscope to corroborate the positions of the datums
258 described within this work. The selected foraminifera were placed on a piece of carbon tape,
259 and then coated with a 4 nm thick coating of carbon or platinum prior to imaging.

260

261 **Stable isotope analysis**

262 Three species of benthic foraminifera (*Planulina wuellerstorfi*, *Cibicidoides mundulus*, and
263 *Cibicidoides robertsonianus*) and one species of planktic foraminifera (*Globigerinoides ruber*)
264 provide a stable isotope chemostratigraphy for Site U1396. *P. wuellerstorfi* was most common
265 until 25 m CCSF-A (~ 1.5 Ma), although it was absent in some samples throughout this interval.
266 In these cases, *C. mundulus* was used in place of *wuellerstorfi*, but within the upper ~ 10 m
267 *mundulus* was also scarce, and *C. robertsonianus* was used instead. Within the top 7 m, sample
268 volume was reduced (to alleviate the depletion of the core with the 5-cm resolution), and so a

269 mixture of all three species was used. *Globigerinoides ruber* was used through the Brunhes chron
270 to address low variability within the benthic $\delta^{18}\text{O}$ record (see below).

271 Preservation state was variable through the study interval. Specimens were graded on a
272 'pristine' - 'frosty' - 'bad' scale. Pristine individuals were glassy, with no infilling. Frosty
273 individuals were opaque, or had mild infilling. 'Bad' individuals, which were only used in rare
274 instances where there was no other choice, had overgrowths, broken final chambers, or
275 moderate infilling. The best-preserved individuals were used for isotopic analysis, though tests
276 were generally 'frosty' throughout the study interval. A table of $\delta^{18}\text{O}$ values, ages, species, and
277 preservation grade can be found in the supplemental information. The only general trend
278 identified in preservation was a gradual decrease in the frequency of well-preserved benthic
279 foraminifera with increasing depth, though examples of good preservation were found near the
280 base of Site U1396.

281 *Planulina wuellerstorfi* was typically used in preference to either *Cibicidoides* species. 41
282 samples contained sufficient individuals from two species to allow isotopic offsets to be
283 generated between the species. The number of individuals analyzed in each sample varied (see
284 supplemental information), but was typically only three to four, due to the large mass of the
285 benthic tests. Approximately nine individuals of planktic *Globigerinoides ruber* were used in each
286 analysis. The majority of samples were run at the University of Massachusetts-Amherst Stable
287 Isotope Laboratory on a Finnigan Delta XL+ with a Kiel III automated carbonate preparation
288 system (>7 mbsf; these are in black, red, and brown on Figure 4). All data are reported in delta
289 notation against the VPDB standard. Replicated analyses of UMass house standard material
290 have a 1σ error of 0.08‰ $\delta^{18}\text{O}$. The rest of the samples were run at the National Oceanography

291 Centre, Southampton using a Europa GEO 20-20 mass spectrometer with an automatic
292 carbonate preparation system (0-7 mbsf; orange on Fig. 4).

293

294 **RESULTS**

295 **Astrochronology**

296 Brightness (L^*) in the shipboard color reflectance dataset (Expedition 340 Scientists,
297 2013) was found to have cyclicity on orbital periods (Fig. 3), despite noise present outside of the
298 expected orbital signals. Tuning resulted in mild offsets from the sedimentation rate derived
299 from linearly interpolating between paleomagnetic reversals, and there appears to be a
300 continuous record of sedimentation at this site. It should be noted that tuning was performed
301 attempting to fit all available chronostratigraphic information and the results of Wall-Palmer et
302 al. (2014) (See 5. Discussion). Most of the deviations from paleomagnetically-derived ages are
303 within the 0-50 kyr range.

304

305 **Benthic isotope values**

306 Stable isotope results largely agree with the expected general pattern of glacial-
307 interglacial cycles, with variability decreasing with depth. There is a gradual trend towards
308 increasing $\delta^{18}\text{O}$ values, with a mean value of $\sim 2\text{‰}$ for 100-150 CCSF-A, increasing to $\sim 2.5\text{‰}$ for
309 50-10 CCSF-A. Strong ($>1\text{‰}$) variability in the record is seen beginning around 30 mbsf until 0
310 mbsf, with a marked step towards higher values observed at ~ 80 CCSF-A.

311 The offset in $\delta^{18}\text{O}$ values between the three species was calculated (Figure 5). Most $\delta^{18}\text{O}$
312 offsets were within the propagated instrumental error for the two $\delta^{18}\text{O}$ measurements ($\sim 0.1\text{‰}$

313 for each measurement, and therefore $\sim 0.14\%$ for offsets). The mean offset between *Planulina*
314 *wuellerstorfi* and *Cibicides mundulus* was $\sim 0.062\%$ (n=25), while *Cibicides mundulus* and
315 *Cibicides robertsonianus* was $\sim -0.011\%$ (n=14). Only two samples contained both *Planulina*
316 *wuellerstorfi* and *Cibicides robertsonianus*, and they displayed a mean offset of -0.105% . No
317 stratigraphic trends were noted with respect to the offsets.

318 *Planulina wuellerstorfi* was most commonly used within 150-80 CCSF-A, with *Cibicides*
319 *mundulus* and *C. robertsonianus* largely used until ~ 7 mbsf, and, due to smaller sample sizes, a
320 mix of benthic all three species above 7 mbsf. When *P. wuellerstorfi* was not available (above 80
321 CCSF-A), *Cibicides mundulus* was used to supplement, using the offset value generated in this
322 study ($\sim 0.062\%$). In the case where *Cibicides robertsonianus* was the only possible choice, the
323 offsets from *P. wuellerstorfi* to *C. mundulus* and *C. mundulus* to *C. robertsonianus* were used to
324 calculate the composite value (green line, fig. 5A).

325 Benthic foraminiferal $\delta^{18}\text{O}$ results follow the trends established by the LR04 benthic
326 foraminiferal stack (Lisiecki and Raymo, 2005). Although the sampling resolution within this
327 study is lower than that of Wall-Palmer et al. (2014), similar trends can be identified between
328 the planktic and benthic $\delta^{18}\text{O}$ records. Figure 4 presents the correlations between the
329 astrochronologically-derived ages and the LR04 stack (grey lines). Several intervals were not
330 correlated, mainly due to data-resolution issues, but also due to the obscuring of MIS cycles
331 through other means (see discussion about low benthic $\delta^{18}\text{O}$ variability below). Those include
332 around MIS 55 (~ 1.6 Ma) and around KM2 (~ 3.1 Ma). There are also several suggested changes
333 to the interval correlated by Wall-Palmer et al. (2014), which are discussed below.

334

335 **Biostratigraphy**

336 The majority of the datums from Wade, et al. (2011) were found within the sediments at
337 Site U1396 (Table 1, Figure 6). Only *Globorotalia hirsuta*, *Globorotalia hessi*, *Globorotalia excelsa*,
338 *Globoturborotalia apertura*, *Globoturborotalita woodi*, and *Globoturborotalita decoraperta* were not
339 found, or were found in such sporadic occurrences they had limited biostratigraphic utility.
340 *Pulleniatina* was not split into distinct species, instead only the presence or absence of
341 *Pulleniatina* spp. was noted. The order of primary datums was found as expected from youngest
342 to oldest: Top *Globorotalia tosaensis*, T *Globigerinelloides fistulosus*, T *Globorotalia miocenica*, T
343 *Dentoglobigerina altispira*, T *Sphaeroidinellopsis seminulina*, T *Globorotalia margarita*, and lastly T
344 *Globoturborotalita nepenthes*. *Globigerinelloides fistulosus* was found only sporadically and was
345 found above the expected range by ~0.5 Myr. *Globorotalia tosaensis* has only a ~100 kyr
346 difference between the U1396 top and the calibrated age, but otherwise the few biostratigraphic
347 species within the Pleistocene are found well outside their expected ranges (see 5. Discussion).
348 Within the Pliocene, the ranges of *G. miocenica*, *D. altispira*, *S. seminulina*, *G. margarita*, and *G.*
349 *nepenthes* all fit very closely to their expected ranges as calibrated by Wade et al. (2011).

350 Secondary datums T *Globoturborotalita obliquus*, T *Globorotalia exilis*, B *Globorotalia*
351 *truncatulinooides*, T *Globorotalia limbata*, T *Globorotalia pertenuis*, B *Globorotalia tosaensis*, B *Globorotalia*
352 *miocenica*, T *Globorotalia plesiotumida*, and B *Globorotalia exilis* were all found close to their
353 calibrated ages. The bioevents Reappearance and Disappearance of *Pulleniatina* were also
354 extraordinarily close to their calibrated ages. In particular, several of the menardellid species
355 (e.g., *G. exilis*) record substantial fluctuations in their populations, so their adherence to the

356 calibrated ages is surprising, but a positive indicator of the robustness of the planktic
357 foraminiferal datums.

358 Several secondary datums, as might be expected, did not conform as precisely to the
359 expected ages. T *Globorotalia flexuosa* was observed within the top sample, and its base (B G.
360 *flexuosa*) was found ~1.3 myr earlier than expected. The local top for *G. extremus* was 800 kyr
361 younger than it was expected. T *Globorotalia multcamerata* was ~400 kyr younger than the
362 expected age, but as mentioned previously, all menardellids were subject to substantial
363 fluctuations in population. B *G. miocenica* appears within the U1396 sediments ~200 kyr older
364 than its calibrated age, while B *G. pertenuis* appears 500 kyr older than the calibrated base. T
365 *Sphaeroidinellopsis kochi* occurs ~300 kyr younger than the calibrated age.

366 **Hiatuses**

367 Shipboard chronostratigraphy suggested a gradually decreasing sedimentation rate
368 towards the present (Expedition 340 Scientists, 2013). It also suggested a largely continuous
369 section, without apparent hiatuses. Biostratigraphy largely agrees with the paleomagnetically-
370 derived sedimentation rates, and clustering of biostratigraphic datums, as would be
371 characteristic of a hiatus, is not observed in the U1396 sequence. Although hypothetically
372 evolutive harmonic analysis can be used to identify hiatuses (Meyers and Sageman, 2004), the
373 use of such a large window (140-kyr) and the amount of noise within the signal makes this
374 impossible at Site U1396. Astrochronology suggests that there are instances of lowered
375 sedimentation rate. In the absence of strong evidence for hiatuses, the U1396 benthic and
376 planktic $\delta^{18}\text{O}$ isotope time series was correlated to marine isotope stages as if there were no
377 hiatuses.

378

379 DISCUSSION

380 Brunhes stratigraphy

381 This study continues much of the data collection begun in Wall-Palmer et al. (2014). In
382 doing so, some conflicting age diagnostic criteria were revealed within tens of cm from the base
383 of the Wall-Palmer study, suggesting a revision of that chronostratigraphy may be necessary.
384 For example, Wall-Palmer et al. (2014) used a %*Globorotalia menardii-tumida* zonation scheme
385 (Ericson & Wollin, 1968; Kennett and Huddlestun, 1972) successfully employed in the region
386 (e.g., Reid et al., 1996; Le Friant et al., 2008). This scheme relies on the relative abundance of
387 *Globorotalia menardii* or *Globorotalia tumida* (the majority of the flat, keeled planktic foraminifera
388 within these sediments). The zonations are described as abundant (Z, X, V, and T) or not
389 abundant (Y, W, and U). Distinguishing between 'abundant' and 'not abundant' is not always
390 obvious in these sediments (Figure 7, W to early V). Here we continued the %*G. menardii-tumida*
391 counts down to the Brunhes-Matuyama reversal, identifying distinct proportion changes
392 centimeters below the lowest sample analyzed by Wall-Palmer et al. (2014). This extension of
393 %*G. menardii-tumida* data, as well as the longer perspective of the entire Brunhes chron, creates
394 uncertainty for some aspects of the chronostratigraphy of Wall-Palmer et al. (2014).

395 The most important chronostratigraphic control used by Wall-Palmer et al. (2014) in the
396 lower part of their study interval was the base (B) of *Emiliana huxleyi*. B *Emiliana huxleyi* globally
397 occurs within MIS 8 (~0.27 Ma) or MIS 9 (~0.29 Ma; Ogg et al., 2014). It was identified at ~6.9 m
398 with SEM imaging (Wall-Palmer et al., 2014), but other studies (Aljahdali, 2013, unpublished
399 Masters Thesis, Florida State University) place the first occurrence much higher (~3 m). In

400 addition, the planktic foraminifera datum for Biozones PT1a/1b, *T. G. tosaensis* (~0.61 Ma; Wade
401 et al., 2011), was determined to be slightly below the *E. huxleyi* datum. Within the original
402 publication, this was suggested to be a regional difference in extinction, with *T. G. tosaensis*
403 occurring at MIS ~8 (0.27 Ma), which is ~340 kyr offset from its calibrated age (Wade et al.,
404 2011). It should be noted that several species discussed later have large offsets from the Wade et
405 al. (2011) biozonation scheme at this site.

406 The following discussion highlights the discrepancies noted within the Brunhes chron.
407 However, the stratigraphy presented in Wall-Palmer et al. (2014) is largely convincing when
408 directly compared with previous studies within the area (Le Friant et al., 2008; Trofimovs et al.,
409 2010). Despite the comparatively low resolution of the new benthic and planktic foraminifera
410 oxygen isotope stratigraphy presented here, the longer perspective of this study highlights
411 discrepancies that are not apparent in those previous studies, which all focus on the uppermost,
412 <~250 kyr seafloor sediment. In addition, oxygen isotope values from MIS 3 to MIS 4 in Wall-
413 Palmer et al. (2014) rise when most records (e.g., Martinson et al., 1984; Lisiecki and Raymo,
414 2005; Le Friant et al., 2008) demonstrate lowering values. There is also a prominent negative
415 shift within MIS 6 (~2‰), when global records (e.g., Martinson et al., 1984; Lisiecki and Raymo,
416 2005) are largely constant. That shift which was correlated to a negative shift in the CAR-MON
417 2 record (Le Friant et al., 2008), but the magnitude at CAR-MON 2 was only ~1‰. In addition,
418 at CAR-MON 2, the MIS 3 to 4 values when correlated with the global stack, rather than the
419 apparently aberrant changes seen in the Wall-Palmer et al. (2014) correlation.

420 There is an additional unsatisfactory correlation in regards to the %*Globorotalia menardii*-
421 *tumida* zonation. In figure 7, the orange bands are zones which should have higher %*G.*

422 *menardii-tumida*, whereas white zones should be lower. Although there is a slight shift at the
423 CAR-MON 2 X Zone to younger ages, the zonal boundaries and abundances are largely as
424 expected (Le Friant et al., 2008), suggesting that a good fit is possible within the region. Within
425 the Wall-Palmer et al. (2014) scheme the divisions between various zones conform poorly to the
426 expected zonation scheme (Fig. 7). For example, Zone X, which should be 'high abundance' has
427 lower abundance on average than Zone W, which should be 'low abundance'.

428 Three possibilities may explain the observed discrepancies (*B. E. huxleyi*, *T. G. tosaensis*,
429 $\delta^{18}\text{O}$ magnitudes, and %*G. menardii-tumida*). First, if the revised stratigraphy proposed in Fig. 7
430 is incorrect and the Wall-Palmer et al. (2014) stratigraphy is correct, the Aljhdali datum is 3 m
431 too high, and there is a condensed section encompassing MIS 9 to 13. This then suggests that
432 MIS 3 has a $\delta^{18}\text{O}$ value roughly equivalent to MIS 5 or 7, rather than the much more positive
433 value expected (Martinson et al., 1984; Lisiecki and Raymo, 2005). Although some differences
434 could be attributable to local effects (sea surface temperature or salinity), because these values
435 are derived from the mixed-layer dwelling *Globigerinoides ruber*, the values from CAR-MON 2
436 are similar to those expected (Le Friant et al., 2008). As described above, MIS 6 (as identified by
437 Wall-Palmer et al., 2014) also has a 'spike' of double the magnitude observed elsewhere. Also,
438 the %*G. menardii-tumida* zonation then has a much weaker connection to the glacial-interglacial
439 cycles. In addition to the previously described difficulties in Zones Y-W, the predicted high
440 abundances through zone V are entirely absent. This is in direct opposition to the CAR-MON 2
441 core, where the expected higher values for Zone X are present (slightly later than expected,
442 however), whereas the low absence that defines Zone W is typified by 0%, rather than the
443 increase of ~3-4% observed in the Wall-Palmer et al. (2014) correlation. Despite the poor

444 chronostratigraphic fit described above, it should be stated that *B. E. huxleyi* is an exceptionally
445 well-established datum, with a consistently robust MIS 8 appearance within the tropics
446 (Thierstein et al., 1977; Ogg et al., 2012), and as such, should have a higher chronostratigraphic
447 priority than a comparably less precise abundance-based zonation scheme. There are
448 lithostratigraphic correlations that appear to support the Wall-Palmer et al. (2014)
449 chronostratigraphic correlations (Coussens et al., 2016), but they lack the longer time-series
450 present at U1396.

451 Second, if the Wall-Palmer et al. (2014) datum is valid and the Aljahdali datum is
452 incorrect, and the rest of the Wall-Palmer et al. stratigraphy is not correct, then this would
453 represent a >100 kyr earlier origination for *E. huxleyi* than previously identified. As stated
454 above, *B. E. huxleyi* has a remarkably globally synchronous first appearance at MIS 8 (Thierstein
455 et al., 1977), whereas the Wall-Palmer stratigraphy suggests it occurred within MIS 13. This
456 scenario to solve the discrepancy seems unlikely. A possible explanation for the *E. huxleyi*
457 datum presented by Wall-Palmer et al. (2014) may be due to downhole contamination, making
458 the Aljahdali *B. E. huxleyi* datum the first *in situ* occurrence (MIS 8; Thierstein et al., 1977; Ogg et
459 al., 2012). The sample cited for the *B. E. huxleyi* by Wall-Palmer et al. (2014) (Sample 340-U1396-
460 1H-5, 90-91 cm) only contained rare *E. huxleyi*, while the only other samples examined above
461 (Samples 340-U1396-1H-1, 1-2 cm and 340-U1396-1H-1, 30-31 cm) contained abundant *E.*
462 *huxleyi*. While the sediments used for SEM analysis were procured in the proper fashion
463 (sample edges were trimmed to minimize down-hole contamination, for example), the rarity of
464 *E. huxleyi* within Sample 340-U1396-1H-5, 90-91 cm possibly suggests that they were not *in situ*.
465 This could account for the ~3 m difference between the two studies.

466 By removing the Wall-Palmer et al. (2104) *B. E. huxleyi* control on the chronostratigraphy,
467 we can then fit to several other chronostratigraphic systems to these observations (Figure 7). For
468 example, *G. menardii* Zones X and V now fit with their expected abundances (Fig. 7) and MIS 6
469 no longer has a negative $\delta^{18}\text{O}$ excursion (MIS 6.4 in Wall-Palmer et al., 2014). Instead, that
470 double peak has been moved to the expected position in MIS 7 and *B. Globorotalia tosaensis* also
471 has a smaller offset to the calibrated age (Table 1). It should be noted that this revision uses data
472 that was excluded from Wall-Palmer et al. (2014) because it was within event bed B1/2. There
473 are a greater number of keeled foraminifera within this flow, as seen within the X Zone defined
474 by this study (~25%, Fig. 7). It is difficult to explain the preferential incorporation of keeled,
475 thermocline-dwelling planktic foraminifera (from ~5% up to ~25%) within a bioclastic flow
476 sourced from shallower depths, where those taxa are rare to absent. In fact, the opposite should
477 be true, and shallow-dwelling benthics and mixed-layer planktic foraminifera should
478 overwhelm the *menardii* and *tumida* percentages, making them even rarer. Additionally, this
479 would be during a time interval when those taxa are especially uncommon. Very different
480 hydrographic properties, however, between the keeled and non-keeled make it possible for this
481 apparent anomaly to be due to some sort of sorting phenomena related to the flow. The
482 remainder of this work employs this last hypothesis (fig. 7) as the age model. Despite this
483 interim conclusion, the interval between MIS 9-13 remains unsatisfactory due to the limited
484 isotopic variation (although a hypothesis to explain this observation is discussed later).

485

486 **Biostratigraphy**

487 Relative to the calibration of Wade et al. (2011), very few of the Pleistocene datums at
488 Site U1396 were found where they were expected. *Globorotalia tosaensis* and *G. obliquus* appear to
489 have a robust calibration from the Caribbean perspective, but this may be a function of the
490 limited number of datums within the Pleistocene, relative to Pliocene. Both of the youngest
491 datums, T *Globorotalia flexuosa* and B *G. calida*, appear to have substantially different ranges than
492 the Wade calibration. For B *G. calida*, this is possibly due to regional differences between the
493 Pacific Ocean (the source of the Wade calibration is from DSDP Leg 135; Chaproniere et al.,
494 1994) and the Caribbean Sea. *Globorotalia flexuosa* is also found far earlier than expected. The
495 diagnostic feature of *G. flexuosa* is a $\sim 90^\circ$ twist on the final chamber, with the rest of the gross
496 morphology resembling an intermediate form between *Globorotalia menardii* and *Globorotalia*
497 *tumida*. Figure 6 (green box) depicts *G. tumida* and *G. flexuosa*, from the sample containing B *G.*
498 *flexuosa*. Also within that sample, very rarely, was an aberrant form of *G. flexuosa* or *G. tumida*
499 with a final chamber appearing to start at 90° to the coiling axis, then twisting back equatorially.
500 This could speculatively be seen as evidence that the '*flexuosa*' form is a simple mutation from
501 the *Globorotalia menardii* sensu stricto, which induces an $\sim 90^\circ$ torsion in the final chamber, rather
502 than being a true biological species. Further work could elucidate if there is an ecological
503 affinity to the '*flexuosa*' form, or if it has a stochastic appearance in the fossil record, as would be
504 expected of a random mutation of the form. Both of these species, *G. flexuosa* and *G. calida*, have
505 recognition issues as they progress through ontogeny. An adult *calida* resembles a juvenile
506 *Globigerinella aequilateralis*, while *G. flexuosa* without the final chamber could be identified as a *G.*
507 *tumida* or *G. menardii*. As impoverished as the Pleistocene is for datums, these are still poor
508 characteristics for biostratigraphic marker taxa.

509 These two biostratigraphic taxa were used repeatedly shipboard during Exp. 340,
510 because the majority of the sites recovered were younger than any primary planktic foraminifer
511 marker datum, and so these secondary datums had to be regularly employed. Finding these two
512 taxa outside of their expected ranges at Site U1396 calls into question many of the
513 biostratigraphically-derived ages for other sites drilled during Exp. 340. Many of those other
514 sites, however, also have nannofossil biostratigraphic datums. Those ages, which were
515 supported by the *B. E. huxleyi*, the nearest nannofossil datum to *B. G. calida* (calibrated age), are
516 still considered to be valid under this study.

517 There are comparatively more datums within the Pliocene than the Pleistocene that
518 conform to expectations. Closest to the Pliocene/Pleistocene boundary is *B. Globorotalia*
519 *truncatulinoides*, which might better be employed as the PL6/PT1b zonal marker than *T*
520 *Globigerinoides fistulosus*. The difference between the Pliocene/Pleistocene boundary and the top
521 of PL6 would only change ~120 kyr, and *G. truncatulinoides* is more common, at least in these
522 sediments, than *G. fistulosus*. Both taxa are easily recognizable, the only advantage that *fistulosus*
523 has over *truncatulinoides* is that the projections from a *fistulosus* test are readily identifiable even
524 when broken. Most of the menardellid Top calibrations were accurate at U1396, excluding *T*
525 *Globorotalia multicamerata*. The spacing between events at U1396, however, was condensed, all
526 taking place within chron C2r. The *B. G. fistulosus* occurs later than expected, and within the
527 wrong biozone. This species is very sporadic throughout its entire range (including the upper
528 portion of the range), making both the first and last occurrences uncertain. The *T* and *B. G. exilis*
529 were observed in close proximity to the expected age, though not always within the biozone
530 expected, due to deviations in other marker taxa.

531
532
533
534
535
536
537
538
539
540
541
542
543
544
545
546
547
548
549
550
551
552

Sedimentation

age scheme mismatch

This study employs three different age models, a paleomagnetic reversal record, an astrochronologically-tuned record (between paleomagnetic datums), and marine isotope stage correlations. These different methods have individual strengths and weaknesses. Paleomagnetic reversal ages are precisely known and are relatively well defined in the U1396 record (Hatfield 2015), but during periods of stable polarity the age model is a simple linear interpolation between reversals. Astrochronology provides variable accuracy and precision. The analysis utilizes a number of different parameters, like window size or interpolation step, that all change how responsive the resulting age model is to hiatuses or changes in sedimentation rates, or the upper and lower limits of detectable frequencies. Lastly, MIS correlation is generally precise provided that all marine isotope stages are present and confidence in the result is increased when constrained by the paleomagnetic reversal record. It also has the advantage, if the data-resolution is high enough to detect them, that extremely abrupt sedimentation rate changes can be observed. The same hypothetical abrupt sedimentation rate would be missed by paleomagnetic ages if it were within a single normal or reverse chron. Similarly, the change in sedimentation rate would be smoothed by astrochronology if the window size were not small enough to detect it. However, if all marine isotope stages are not present, or if data density is poor, then correlation becomes less accurate using this method. Because of the three different characteristics of these age models, it is possible to demonstrate the advantages of the different models of age estimations by looking at their offsets.

553 The three non-biostratigraphic age schemes agree well, as seen in Figure 8, when
554 excluding the Brunhes chron (see section 5.1). Figure 9 presents the differences in ages between
555 the various methods of age estimation, paleomagnetically-derived minus marine isotope stage
556 (Mag-MIS) and paleomagnetically-derived minus astrochronologically-derived (Mag-A). If the
557 Brunhes chron is excluded, the Mag-MIS offset is typically larger than Mag-A. This suggests
558 that the astrochronology method is underestimating high sedimentation rates and
559 overestimating low sedimentation rates, if we assume that the MIS ages are near-instantaneous
560 estimates of the sedimentation rate. In intervals where Mag-MIS is smaller than Mag-A, the MIS
561 age seems to be reacting to changes in sedimentation rate more quickly than the
562 astrochronologically-derived ages. Again, this is a weakness of this particular astrochronologic
563 age model, likely due to the large window size, which imparts a 'lag' on the changes in
564 sedimentation rate. A larger window size would mix frequencies over a larger interval, and so
565 react more slowly to changes in sedimentation rate while a smaller window size would react
566 more quickly. Again, the larger window-size was used here to account for the noise in the
567 dataset.

568 All offsets between the various age models were generally smaller than the time
569 between isotope stages. This suggests that although the above discussion is valid, the
570 paleomagnetically-derived ages are robust, and eliminating the 'tuning' step within the
571 methods would likely have not changed the MIS-correlations. This also suggests that this is a
572 continuous section, excluding perhaps some portion of the Brunhes chron.

573

574 *sedimentation rates*

575 The sedimentation rate is calculated in several different forms. First, a linear
576 sedimentation rate was calculated from the paleomagnetic reversal record, both including
577 volcanics and without (Fig. 10). The difference between these two, or the volcanic accumulation
578 rate, is in purple. The non-volcanic, or hemipelagic, sedimentation rate curve is different from
579 previous studies. Shipboard chronostratigraphy described a roughly monotonic decrease in
580 sedimentation rate from 0 Ma to ~4.5 Ma (Expedition 340 Scientists, 2013), which is seen in the
581 total sedimentation rate (Fig. 10). When the thickness of the volcanically-sourced sediments is
582 removed (Fig. 10), the monotonic decrease in rate disappears and the sedimentation rates
583 resemble a step-function. When viewed as a step function, sedimentation rates are ~4 cm/kyr
584 until ~2.2 Ma and ~2 cm/kyr thereafter, partially owing to the increasing thickness of the
585 volcanically-sourced beds from ~3.5-4.5 Ma (purple line, Fig. 10), which account for ~1 cm/kyr
586 of the sedimentation rate. Alternatively there is a gradual decline in sedimentation rate from
587 ~3.5 to ~2.1 Ma, with higher rates before and lower rates after. Either interpretation removes the
588 monotonic increase seen in the sedimentation rate that includes both volcanic and hemipelagic
589 sedimentation.

590 The sedimentation rate constructed from the marine isotope correlations is much more
591 variable than the paleomagnetically-derived sedimentation rates, but still follows the
592 approximate trends defined by the paleomagnetic rates. The rates are particularly variable prior
593 to 2 Ma. Rates are ~6 cm/kyr until ~3.65 Ma, then drop to ~4 cm/kyr from ~2.15-3.65 Ma. There
594 is a slow decline in the rates from ~4 cm/kyr to ~2 cm/kyr from ~2.5- ~1.5 Ma. There is a pulse
595 of sediment roughly coincident with the middle Pleistocene Transition (MPT), with rates
596 varying between ~4 and <1 cm/kyr afterwards. Brightness (L^*) shows a particularly good

597 agreement with the sedimentation rates. Figure 10 depicts the sedimentation rates, with the
598 black line representing a running mean of L^* with a 100 kyr window to remove higher
599 frequency cycles and examine only the longer-term trends. There is a significant correlation
600 between sedimentation rate and L^* (See fig. 10 inset, $n = 87$, Pearson's $r = -0.5416$, p value <
601 0.001). This connection suggests that the lighter sediments (higher L^* values) were deposited at
602 a slower rate than the darker sediments (lower L^* values). $\text{CaCO}_3\%$ data, from shipboard
603 geochemistry, shows a weak correlation to the L^* values throughout the entire record. Although
604 shipboard sampling for CaCO_3 measurements attempted to avoid the influence of volcanic
605 sediments and sample purely hemipelagic sedimentation, the distinct possibility that carbonate-
606 free volcanic material, in the form of cryptotephra (dispersed ash), may be influencing the
607 $\text{CaCO}_3\%$ data was suggested by Expedition 340 Geochemistry (Expedition 340 Scientists, 2013).

608

609 *local volcanism / regional effects*

610 There are several possible explanations for the L^* to sedimentation rate correlation. First,
611 the additional input of dispersed volcanogenic sediment could strongly affect sedimentation
612 rate. The 3.5-4.5 Ma interval has ~ 1 cm/kyr observed volcanic sedimentation, whereas the
613 sedimentation is ~ 4 cm/kyr overall. If we assume, for the sake of discussion, that the flux of
614 purely hemipelagic sediment is constant throughout the entire interval at ~ 2 cm/kyr (~ 0 -2 Ma
615 rough average sedimentation rate), there is ~ 1 cm/kyr of unaccounted for sedimentation in the
616 3.5-4.5 Ma interval. As the observed volcanically-derived sedimentation is highest throughout
617 this interval, it seems possible that the undetected dispersed ash, or cryptotephra (e.g. McCanta
618 et al., 2015), throughout that interval may also be high. The lower L^* value agrees with elevated

619 cryptotephra, as dispersed ash would darken the surrounding sediments. There are pulses of
620 volcanic sediment at ~1.9 Ma which also coincide with inflections in the brightness. This
621 hypothesis, however, does not agree with the land-based local volcanic history. The Silver Hills
622 Volcano on Montserrat was active ~ 2.6 to ~1.2 Ma (Harford et al., 2002), the oldest land-based
623 date for volcanic activity on Montserrat, and the general trend through this interval at Site
624 U1396 is one of increasing brightness and presumably less volcanic ash and other volcanoclastic
625 sediments. Although the volcanogenic sediments could be sourced from elsewhere (e.g., Palmer
626 et al., 2016), and Montserrat is probably older than just the onland ages, it seems likely that
627 these growth phases of subaerial Montserrat (Fig. 10) should have a substantial impact on
628 U1396. If a hypothesis of the sedimentation rate changes being purely volcanically-forced is
629 true, then one would expect that the growth of the nearest volcano to have an impact. Rather,
630 the data suggest less volcanic influence, or at least slower sedimentation rates, as Montserrat
631 grows larger.

632

633 *gateway changes*

634 The closure of the Isthmus of Panama had a profound effect on the oceanography of the
635 Caribbean Sea. In particular, bottom water connection with the Pacific Ocean ceased by ~4.5 Ma
636 (Keigwin, 1982; Haug and Tiedemann, 1998). Other portions of the Central American Seaway
637 (CAS) history are controversial (for a discussion see Molnar, 2008), owing to the prolonged
638 nature of the closure, and/or the possibility that sea level changes derived from glacial-
639 interglacial cycles could have closed and opened the gateway repeatedly (e.g., Groeneveld et al.,
640 2014). There is evidence that there is no more oceanographic exchange through the CAS by ~4.2

641 Ma (e.g., Jain and Collins, 2007), although other authors place 'final closure' later (~3.2-3.6 Ma;
642 Haug and Tiedemann, 1998). Land animal exchange between the continents is observed at 2.7
643 Ma, offering a strict youngest-limit to the closure history. At 4.2 Ma there is a substantial drop
644 in productivity recorded by benthic foraminiferal assemblages and $\delta^{13}\text{C}$ time series at Site 999
645 (Jain and Collins, 2007). Chaisson (2003) observed a distinct change in menardellid evolution
646 between the Atlantic and Pacific Oceans, with the Caribbean Sea forms occupying higher and
647 more oligotrophic conditions. Both productivity and menardellid evolution are linked the CAS
648 closure, which is thought to displace the locus of productivity and upwelling to the Pacific
649 Ocean while the Caribbean Sea experienced growth of oligotrophic conditions. This expansion
650 of oligotrophic conditions is also seen during the interval of highly variable, or 'pulsed'
651 sedimentation rates at U1396. The hemipelagic sediments at U1396 are largely biogenic so there
652 must be a link between productivity and sedimentation rate. This link is not as simple as higher
653 productivity equals higher sedimentation rate because factors like bottom water corrosiveness,
654 siliceous vs. carbonate productivity, or bottom water current strength (among many others)
655 may also alter the sedimentation rate. The confluence of oligotrophic indicators from Site 999
656 and pulsed rates at Site U1396 suggest a possible, but counterintuitive, link.

657 The lower L^* values with higher sedimentation rates could suggest that biogenic silica
658 pulses are driving the sedimentation in the lower Pliocene of Site U1396. The sedimentation rate
659 also appears to possibly contain obliquity-forced cycles during the volatile interval. An obvious
660 alternative explanation for the L^* values is volcanic sedimentation, but it is difficult to connect
661 obliquity cycles with volcanoclastic sedimentation. Obliquity cycles have been observed in
662 productivity indicators at other locations during the Plio-Pleistocene (e.g., Bolton et al., 2010).

663 The link at Site U1396, however, is highly speculative. The correlations between the $\delta^{18}\text{O}$ U1396
664 data and the MIS LR04 stack is, through the highly variable sedimentation rate interval, based
665 on smaller changes in $\delta^{18}\text{O}$ because of the smaller glacial-interglacial changes at those times.
666 The time interval between correlation points is also fairly small, and so minor changes in the
667 points used for correlations could produce substantial impacts on sedimentation rates. The high
668 variability is, however, still seen in the astrochronologically-derived sedimentation rates (not
669 shown). The extreme swings in sedimentation rate also suggest that even if MIS stages were
670 moved by tens of cm the magnitude of the pulses in rate may change, the pulses would remain.
671 The high rates also do not correspond to either extreme glacials or interglacials. Indeed,
672 indicators for high seasonality were observed in the benthic analysis at Site 999 (Jain and
673 Collins, 2007) prior to the final closure at ~ 4.2 Ma. The pulses in sedimentation may indicate
674 that Site U1396, closer to the equatorial Atlantic Ocean, experienced elevated productivity
675 longer than at the more central Caribbean Sea Site 999, or that a long-term trend toward more
676 oligotrophic conditions was punctuated by intervals of higher productivity.

677 There are other gateway changes that could have played a role in controlling
678 sedimentation at Site U1396. Mediterranean Outflow Water (MOW) enters the Atlantic Ocean
679 through the Strait of Gibraltar and is an important component of Atlantic Ocean circulation
680 patterns. Evidence from the Gulf of Cadiz, off the Portugal coast, suggests periods of
681 intensification in MOW strength at 0.7-0.9, 2.0-2.4, and 3.0-3.2 Ma (Hernández-Molina et al.,
682 2014). If this water were to flow into the Caribbean Sea at times, MOW would be the deepest
683 water-mass in the Caribbean Sea due to its high salinity, and thus high density. There is an
684 established glacial-interglacial control on the water entering the Caribbean over the past 200

685 kyr, with more corrosive Antarctic Intermediate Water (AAIW) during the interglacials and less
686 corrosive glacial North Atlantic Intermediate Water (or upper North Atlantic Deep Water)
687 during the glacials (Haddad and Droxler, 1996).

688 Kaneps (1979) suggested increases in Gulf Stream strength throughout the Plio-
689 Pleistocene, interpreting a series of hiatuses on Blake Plateau as intervals of high Gulf Stream
690 velocity. The precise timing of the hiatuses, however, is suspect as the ages are based on 1970-
691 era biostratigraphic calibrations (hence the 1-myrr error bars in Figure 10). If Blake Plateau
692 hiatuses and MOW intensifications were roughly synchronous, then MOW flowing into the
693 Caribbean Sea contributed to a strengthened Gulf Stream flow. At Site U1396 there are intervals
694 of elevated carbonate deposition, very roughly coincident, with the Blake Plateau hiatuses and
695 MOW intensifications. This seems counter to the expectation from the literature (e.g., Haddad
696 and Droxler, 1996), as the bottom water bathing Site U1396 would likely be AAIW, a nutrient
697 rich but corrosive water mass. MOW, on the other hand, would be less corrosive, nutrient poor,
698 and warm. The lithostratigraphy from Site U1396 agrees with different water masses bathing
699 the site throughout the Pleistocene. At ~600 ka and again at ~400 ka there are calcareous sand
700 intervals, which are associated with lower sedimentation rate suggesting extensive winnowing
701 removing the fine fraction (discussed in Wall-Palmer et al., 2014). Removing fine sediment
702 would lower the sedimentation rate. These sandy intervals appear to be associated with MIS 15-
703 16 and MIS 10-12. Directly preceding these sandy intervals, the interval from 0.55 to 0.75 Ma is
704 one of low $\delta^{18}\text{O}$ variability in the benthic record. A change in Caribbean Sea bottom water may
705 explain the decreased benthic $\delta^{18}\text{O}$ variability, if it were episodic, only bathing benthic
706 organisms in warm water during glacials, and a relatively cooler water mass during

707 interglacials. This would have the effect of flattening the curve, effectively removing the benthic
708 glacial-interglacial differences in $\delta^{18}\text{O}$ while retaining the observed high planktic $\delta^{18}\text{O}$. While
709 the dates for MOW intensification do not agree with the lower variability in benthic $\delta^{18}\text{O}$, MOW
710 dates are at present poorly constrained (Hernández-Molina et al., 2014). Currently MOW
711 intensification occurs at $\sim 0.7\text{-}0.9$ Ma (Hernández-Molina et al., 2014). Our low $\delta^{18}\text{O}$ variance
712 interval is ~ 150 kyr younger, with low sedimentation rate and winnowing occurring at $\sim 0.7\text{-}0.6$
713 Ma and $\sim 0.5\text{-}0.35$ Ma, but the mismatch could simply be due to poorly constrained dates from
714 the MOW outflow studies. It should be noted that geochemical evidence points to limited MOW
715 influence in the Caribbean during the Plio-Pleistocene (Osborne et al., 2014), that evidence is
716 only from after 2 Ma, well after the hypothesis described above. The above hypothesis is
717 speculative, but remains a possible explanation for a number of different observations that
718 cannot simply be due to volcanoclastic influence at Site U1396.

719 A second pulse of winnowing coincides with MIS 11. However, low benthic $\delta^{18}\text{O}$
720 variability through this interval is likely due to a limited number of $\delta^{18}\text{O}$ values, as the sample
721 resolution shrinks to ~ 50 kyr. While there is similarity between the winnowing pulse at MIS 15
722 and MIS 11, we cannot rule out a data density issue at MIS 11. The planktic record suggests that
723 while MIS 15 benthic variability is limited, MIS 10 and MIS 12 may be missing in a hiatus, as the
724 typical glacial $\delta^{18}\text{O}$ values are missing from both benthic and planktic records.

725 Perhaps a more likely connection from gateway changes to rates of sedimentation is
726 thermohaline circulation. Haug and Tiedemann (1998) demonstrated a link between the salinity
727 contrast, formed by CAS closure, between Pacific and Atlantic Ocean. This contrast, with saltier
728 Atlantic Ocean water, helps to boost formation of North Atlantic Deep Water (NADW), which

729 in turn boosts thermohaline circulation. Several studies have demonstrated this link (e.g., Zhang
730 et al., 2012; Osborne et al., 2014) both in proxy reconstruction and inter-model comparison.
731 Proxy reconstructions, especially the geochemical reconstructions both from oxygen isotope
732 gradients between Pacific and Atlantic basins and other methods (e.g., Osborne et al., 2014),
733 suggest that this was not a simple single increase, that in fact there were multiple fluctuations in
734 the strength superimposed on the long-term trend of increased thermohaline circulation. These
735 fluctuations in thermohaline circulation were of varying duration, but had ~100-kyr scale
736 durations, and so could be some of the variability that is seen in the sedimentation rates at Site
737 U1396, while the longer term trend in quicker bottom water flow would explain the general
738 trend to slower sedimentation rates at U1396 within the upper portion of the record.

739 Increased bottom water current flow due to increased thermohaline circulation, and
740 therefore increased winnowing, is supported by the qualitative core description. There is a
741 change at Site U1396 to more calcareous sand style sedimentation within the upper portion of
742 the record, away from the lower, more ooze-dominated sedimentation of the lower portion.
743 This can be seen most clearly on the CCSF-NV lithologic section on Figure 2. This mean increase
744 in grain size, likely due to winnowing of the fine-grained material, would decrease the
745 sedimentation rate. In fact, as seen in Figure 7, ooze deposition is coincident with increased
746 sedimentation rate during the Brunhes chron, though this depends on the age model.

747

748 Realistically, the observed changes in sedimentation rate and brightness are a mixture of
749 different factors: volcanic input, carbonate and siliceous productivity, and thermohaline
750 circulation. The period from ~3-4 Ma could have been a period of highly variable productivity,

751 driven by obliquity and incomplete construction of the CAS. Thermohaline circulation, as the
752 CAS had not completely closed, could also have been uneven, and sped up and slowed down in
753 fits, as seen in Osborne et al. (2014), leading to the highly volatile rates observed through that
754 interval. As CAS closure became more complete, the increase in thermohaline circulation drove
755 quicker bottom water circulation over Site U1396, leading to increased winnowing and lower
756 sedimentation rates, resulting in the gradual decline in rates observed. Lastly, the low
757 sedimentation rates, with pulses of winnowing, could have been due to the lower productivity
758 and increased thermohaline circulation and thus variation in bottom water character during the
759 0-2 Ma interval. Throughout the entire section, there must be a substantial fraction of the
760 sedimentation rate controlled by volcanoclastic sediment. The volcanic influence here is only
761 constrained somewhat within this study, further work must be done to detail the degree to
762 which there is dispersed ash within the sediments at Site U1396. This analysis provides the first
763 step to understanding the other, non-volcanic, factors contributing the accumulation of
764 sediment at this location.

765

766 CONCLUSIONS

767 1. Site U1396, drilled ~33 km southwest of Montserrat, contains a relatively continuous
768 sequence of Pliocene and Pleistocene sedimentation. There is a general trend to decreasing
769 sedimentation rate towards the present, both in volcanic and non-volcanic sedimentation.

770

771 2. The chronostratigraphy of Site U1396 is based on planktic foraminifer biostratigraphy,
772 calcareous nannofossil biostratigraphy, magnetostratigraphy, astrochronology, and oxygen

773 isotope chemostratigraphy (marine isotope stages). The resulting chronostratigraphy provides a
774 detailed framework to reconstruct the paleoceanography and record of sediment accumulation
775 in the northeastern Caribbean.

776

777 3. A revision of the previous Wall-Palmer et al. (2014) chronostratigraphy is proposed.
778 Here we highlight differences observed in the chonostratigraphic schemes employed and U1396
779 and use the longer perspective of U1396 to develop an alternative hypothesis, which fits better
780 when considering the Brunhes chron as a whole. Although there is a call for further
781 chronostratigraphic investigations, these findings may have dramatic implications for the
782 reconstruction of the volcanic history of Montserrat.

783

784 4. Two biostratigraphic datums used extensively shipboard (*B Globigerinella calida* and *T*
785 *Globorotalia flexuosa*) were found to be unreliable at Site U1396. Use of those datums at other
786 Exp. 340 sites should be restricted to occurrences supported by additional chronostratigraphic
787 information (nannofossils, for example).

788

789 5. There is a strong correlation ($p < 0.001$) between sedimentation rate and L^* (brightness).
790 There is weak correlation between ($p < 0.1$) brightness and CaCO_3 content throughout the entire
791 record, but some intervals of L^* qualitatively appear to be controlled by carbonate content. This
792 suggests that the main phases of Montserrat volcanism may not be contributing strongly to the
793 sedimentation at Site U1396, as the growth of Montserrat (<2.6 Ma) occurs during times of

794 lower sedimentation rates at Site U1396.

795

796 6. Sedimentation rate at Site U1396 (IODP Expedition 340) is likely controlled by a mix of
797 factors, including volcanogenic, lithogenic, and biogenic sediment sources. A series of
798 hypotheses to explain the rates were explored, with connections to Site 999, a more centrally
799 located Caribbean Sea ODP Site, with suggestions for future work to elucidate the direct causes.
800 Highly variable, but consistently elevated, rates of sedimentation are surprisingly high during a
801 period normally considered to be oligotrophic within the Caribbean Sea. It is suggested,
802 therefore, that a more likely cause is due to bottom water conditions, including episodic
803 changes in bottom water flow rates in the Pliocene and increased winnowing into the
804 Pleistocene, associated with CAS closure through the studied interval.

805

806 **Acknowledgements**

807 The authors would like to thank first and foremost the crew and scientific staff of the R/V
808 *JOIDES Resolution*, as well as the rest of IODP staff. This study was funded through an IODP
809 Post Expedition Award to Leckie and Fraass. The ideas here were helped by fruitful discussion
810 within the Leckie Micropaleontology Lab, with Emily Browning, Raquel Bryant, Kendra Clark,
811 Serena Dameron, Adriane Lam, Christopher Lowery, Renata Moura de Mello, and Steven
812 Nathan. They would also like to thank Michael Jercinovic, Craig Astore, Megan Leckie, and
813 Susanna Fraass.

814

815 **References**

816 ALJAHDALI, M.H., 2013. Pliocene-Pleistocene Calcareous Nannofossil Biostratigraphy of Iodp
817 Hole 1396c Adjacent To Montserrat Island In The Lesser Antilles, Caribbean Sea, Plus
818 Experimentally Induced Diagnosis. *Electronic Theses, Treatises and Dissertations*. Paper 7270.

819 BACKMAN, J., RAFFI, I., RIO, D., FORNACIARI, E., and PÄLIKE, H., 2012. Biozonation and
820 biochronology of Miocene through Pleistocene calcareous nannofossils from low and
821 middle latitudes. *Newsletters on Stratigraphy*, 45:221-244.

822 BÉ, A.W.H., and TOLDERLUND, D.S., 1971. Distribution and ecology of living planktonic
823 foraminifera in surface waters of the Atlantic and Indian Ocean. In: FUNNEL, B.M.,
824 RIEDEL, W.R. Eds., *The Micropaleontology of Oceans*, 105-149. Cambridge: Cambridge
825 University Press.

826 BECKER, R.A., WILKS, A.R. (Original S code), R. BROWNRIGG (R version), T. P. MINKA
827 (Enhancements), 2015. maps: Draw Geographical Maps. *R package* version 2.3-11.
828 <http://CRAN.R-project.org/package=maps>.

829 BERGGREN, W.A., and PEARSON, P.N., 2006. Tropical and subtropical planktonic
830 foraminiferal zonation of the Eocene and Oligocene. In: PEARSON, P.N., OLSSON, R.K.,
831 HUBER, B.T., HEMLEBEN, C., and BERGGREN, W.A., Eds., *Atlas of Eocene Planktonic*
832 *Foraminifera*, 29-40. *Cushman Foundation Special Publication* 41.

833 BOLTON, C.T., GIBBS, S.J., and WILSON, P.A., 2010. Evolution of nutricline dynamics in the
834 equatorial Pacific during the late Pliocene. *Paleoceanography*, 25:PA1207.
835 doi:10.1029/2009PA001821

836 CANDE, S.C. and KENT, D.V., 1995. Revised calibration of the geomagnetic polarity timescale
837 for the Late Cretaceous and Cenozoic. *Journal of Geophysical Research*, 100:6093-6095.

838 CAREY, S.N. and SCHNEIDER, J-L., 2001. Volcaniclastic processes and deposits in the Deep-
839 Sea. *Developments in Sedimentology*, 63:457-515.

840 CASSIDY, M., TROFIMOV, J., PALMER, M.R., TALLING, P.J., WATT, S.F.L., MORETON,
841 S.G., and TAYLOR, R.N. 2013. Timing and emplacement dynamics of newly recognised
842 mass flow deposit at ~8-12 ka offshore Soufriere Hills volcano, Montserrat: How submarine
843 stratigraphy can complement subaerial eruption histories. *Journal of Volcanology and*
844 *Geothermal Research*, 253:1-14.

845 CASSIDY, M., WATT, S.F.L., PALMER, M.R., TROFIMOV, J., SYMONS, W., MACLACHLAN,
846 S.E., and STINTON, A.J., 2014. Construction of volcanic records from marine sediment
847 cores: A review and case study (Montserrat, West Indies). *Earth-Science Reviews*, 138:137-155.

848 CHAISSON, W.P. and D'HONDT, S.L., 1999. Neogene Planktonic Foraminifer Biostratigraphy
849 at Site 999, Western Caribbean Sea, in: LECKIE, R.M., SIGURDSSON, H., ACTON, G.D., and
850 DRAPER, G., Eds. *Proceedings of the Ocean Drilling Program, Scientific Results*, 165, 19-56.
851 College Station: Ocean Drilling Program.

852 CHAPRONIERE, G.C.H., STYZEN, M.J., SAGER, W.W., NISHI, H., QUINTERNO, P.J., and
853 ABRAHAMSEN, N., 1994. Late Neogene biostratigraphic and magnetostratigraphic
854 synthesis, Leg 135. In: HAWKINS, J., PARSON, L., ALLAN, J. et al. Eds., *Proceedings of the*
855 *Ocean Drilling Program, Scientific Results*, 135, 857-887. College Station: Ocean Drilling
856 Program.

857 CLARK, P. U., ARCHER, D., POLLARD, D., BLUM, J. D., RIAL, J. A., BROVKIN, V., MIX, A. C.,
858 PISIAS, N. G., and ROY, M., 2006. The middle Pleistocene transition: characteristics,

859 mechanisms, and implications for long-term changes in atmospheric $p\text{CO}_2$. *Quaternary*
860 *Science Reviews*, 25: 3150-3184.

861 COUSSENS, M.F., WALL-PALMER, D., TALLING, P.J., WATT, S.F.L, HATTER, S.J., CASSIDY,
862 M., CLARE, M., JUTZELER, M., HATFIELD, R., MCCANTA, M., KATAOKA, K.S., ENDO,
863 D., PALMER, M.R., STINTON, A., FUJINAWA, A., BOUDON, G., LE FRIANT, A.,
864 ISHIZUKA, O., GERON, T., ADACHI, T., ALJAHDALI, M., BREITKREUZ, C., FRAASS,
865 A.J., HORNBAACH, M.J., LEBAS, E., LAFUERZA, S., MAENO, F., MANGA, M.,
866 MARTINEZ-COLON, M., MCMANUS, J., MORGAN, S., SAITO, T., SLAGLE, A.,
867 SUBRAMANYAM, K.S.V., TAMURA, Y., TROFIMOV, J., VILLEMANT, B., WANG, F., and
868 EXPEDITION 340 SCIENTISTS, 2016. Synthesis: stratigraphy and age control for IODP Sites
869 U1394, U1395, and U1396 offshore Montserrat in the Lesser Antilles. In: LE FRIANT, A.,
870 ISHIZUKA, O., STRONCIK, N.A., and EXPEDITION 340 SCIENTISTS, *Proceedings of the*
871 *Integrated Ocean Drilling Program*, 340. Tokyo: Integrated Ocean Drilling Program
872 Management International, Inc.. doi:10.2204/iodp.proc.340.204.2016

873 CRUTCHLEY, G.J., KARSTENS, J., BERNDT, C., TALLING, P.J., WATT, S.F.L., VARDY, M.E.,
874 HÜHNERBACH, V., URLAUB, M., SARKAR, S., KLAESCHEN, D., PAULATTO, M., LE
875 FRIANT, A., LEBAS, E., and MAENO, F., 2013. Insights into the emplacement dynamics of
876 volcanic landslides from high-resolution 3D seismic data acquired offshore Montserrat,
877 Lesser Antilles. *Marine Geology*, 335:1-15.

878 ERICSON, D.B. and WOLLIN, G., 1968. Pleistocene climates and chronology in deep-sea
879 sediments. *Science*, 162:1227-1234.

880 EXPEDITION 340 SCIENTISTS, 2013. Site U1396, in: LE FRIANT, A., ISHIZUKA, O.,

881 STRONCIK, N.A., and EXPEDITION 340 SCIENTISTS, *Proceedings of the Integrated Ocean*
882 *Drilling Program, 340*. Tokyo: Integrated Ocean Drilling Program Management International,
883 Inc.. doi:10.2204/iodp.proc.340.106.2013

884 GROENEVELD, J., HATHORNE, E.C., STEINKE, S., DEBEY, H., MACKENSEN, A., and
885 TIEDEMANN, R., 2014. Glacial induced closure of the Panamanian Gateway during Marine
886 Isotope Stages (MIS) 95-100 (~2.5 Ma). *Earth and Planetary Science Letters*, 404:296-306.

887 HADDAD, G.A. and DROXLER, A.W., 1996 Metastable CaCO₃ dissolution at intermediate
888 water depths of the Caribbean and western North Atlantic: Implication for intermediate
889 water circulation during the past 200,000 years. *Paleoceanography*, 11:701-716.

890 HARFORD, C.L., 2002. The volcanic evolution of Montserrat using ⁴⁰Ar/³⁹Ar geochronology.
891 In: DRUITT, T.H., KOKELAAR, B.P., Eds., *Geological Society Memoir No. 21: The Eruption of*
892 *Soufrière Hills Volcano, Montserrat, from 1995 to 1999*, 93-113. London: Geological Society of
893 London.

894 HATFIELD, R.G., 2015. Data report: stratigraphic correlation of Site U1396 and creation of a
895 composite depth scale and splice. In: LE FRIANT, A., ISHIZUKA, O., STRONCIK, N.A., and
896 EXPEDITION 340 SCIENTISTS Eds., *Proceedings of the Integrated Ocean Drilling Program, 340*.
897 Tokyo: Integrated Ocean Drilling Program Management International,
898 Inc.. <http://dx.doi.org/10.2204/iodp.proc.340.202.2015>.

899 HAUG, G.H. and TIEDEMANN, R. 1998. Effect of the formation of the Isthmus of Panama on
900 Atlantic Ocean thermohaline circulation. *Nature*, 393:673-676.

901 HERD, R.A. EDMONDS, M., and BASS, V.A., 2005. Catastrophic lava dome failure at Soufriere
902 Hills Volcano, Montserrat, 12-13 July 2003. *Journal of Volcanology and Geothermal Research*,
903 148:234-252. doi: 10.1016/j.jvolgeores.2005.05.003

904 HERNÁNDEZ-MOLINA, F.J., STOW, D.A., ALVAREZ-ZARIKIAN, C.A., ACTON, G., BAHR,
905 A., BALESTRA, B., DUCASSOU, E., FLOOD, R., FLORES, J.-A., FUROTA, S., GRUNERT, P.,
906 HODELL, D., JIMENEZ-ESPEJO, F., KIM, J.K., KRISSEK, L., KURODA, J., LI, B., LLAVE, E.,
907 LOFI, J., LOURENS, L., MILLER, M., NANAYAMA, F., NISHIDA, N., RICHTER, C.,
908 ROQUE, C., PEREIRA, H., GOÑI, M.F.S., SIERRA, F.J., SINGH, A.D., SLOSS, C.,
909 TAKASHIMIZU, Y., TZANOVA, A., VOELKER, A., WILLIAMS, T., and XUAN, C., 2014.
910 Onset of Mediterranean outflow into the North Atlantic. *Science*, 344:1244-1250.

911 JUTZELER, M., WHITE, J.D.L., TALLING, P.J., MCCANTA, M., MORGAN, S., LE FRIANT, A.,
912 and ISHIZUKA, O., 2014, Coring disturbances in IODP piston cores with implications for
913 offshore record of volcanic events and the Missoula megafloods. *Geochemistry, Geophysics,*
914 *Geosystems*, 15:3572-3590, doi:10.1002/2014GC005447.

915 JUTZELER, M., TALLING, P.J., WHITE, J.D.L., and EXPEDITION 340 SCIENTISTS, 2016. Data
916 report: coring disturbances in IODP Expedition 340, a detailed list of intervals with fall-in
917 and flow-in. In: LE FRIANT, A., ISHIZUKA, O., STRONCIK, N.A., and EXPEDITION 340
918 SCIENTISTS, *Proceedings of the Integrated Ocean Drilling Program*, 340. Tokyo: Integrated
919 Ocean Drilling Program Management International, Inc..
920 doi:10.2204/iodp.proc.340.206.2016

921 KANEPS, A.G., 1979. Gulf Stream: Velocity Fluctuations During the Late Cenozoic. *Science*,
922 204:297-301.

923 KEIGWIN, L., 1982. Isotopic paleoceanography of the Caribbean and East Pacific: Role of
924 Panama uplift in late Neogene time. *Science*, 217:350-353.

925 KENNETT, J.P. and HUDDLESTON, P., 1972. Late Pleistocene paleoclimatology, foraminiferal
926 biostratigraphy and tephrochronology, Western Gulf of Mexico. *Quaternary Research*, 2:38-
927 69.

928 LE FRIANT, A., DEPLUS, C., BOUDON, G., FEUILLET, N., TROFIMOV, J., KOMOROWSKI,
929 J.-C., SPARKS, R.S.J., TALLING, P., LOUGHLIN, S., PALMER, M., and RYAN, G., 2010.
930 Eruption of Soufriere Hills (1995-2009) from an offshore perspective: Insights from repeated
931 swath bathymetry surveys. *Geophysical Research Letters*, 37.

932 LE FRIANT, A., LOCK, E.J., HART, M.B., BOUDON, G., SPARKS, R.S.J., LENG, M.J., SMART,
933 C.W., KOMOROWSKI, J.C., DEPLUS, C., and FISHER J.K., 2008. Late Pleistocene
934 tephrochronology of marine sediments adjacent to Montserrat, Lesser Antilles volcanic arc.
935 *Journal of the Geological Society*, 165:279-289.

936 LISIECKI, L.E. and RAYMO, M.E., 2005. A Pliocene-Pleistocene stack of 57 globally distributed
937 benthic $\delta^{18}\text{O}$ records. *Paleoceanography*, 20:PA1003. doi:10.1029/2004PA001071.

938 LOURENS, L.J., HILGEN, F.J., SHACKLETON, N.J., LASKAR, J., and WILSON, D., 2004. The
939 Neogene Period. In: GRADSTEIN, F.M., OGG, J.G., and SMITH, A.G., Eds., *Geological Time*
940 *Scale 2004*, 409-440. Cambridge: Cambridge University Press.

941 MACDONALD, R., HAWKESWORTH, C.J., and HEATH, E., 2000. The Lesser Antilles volcanic
942 chain: a study in arc magmatism. *Earth Science Reviews*, 49:1-76.

943 MARTINSON, D.G., PISIAS, N.G., HAYS, J.D., IMBRIE, J., MOORE JR., T.C., and
944 SHACKLETON, N. J., 1987. Age dating and the orbital theory of the iceages: Development

945 of a high-resolution 0 to 300,000-year chronostratigraphy. *Quaternary Research*, 27:1-29.
946 doi:10.1016/0033-5894(87)90046-9

947 MEYERS, S.R., 2014. astrochron: An R Package for Astrochronology. [http://cran.r-](http://cran.r-project.org/package=astrochron)
948 [project.org/package=astrochron](http://cran.r-project.org/package=astrochron)

949 MEYERS, S.R. and SAGEMAN, B.B., 2004. Detection, quantification, and significance of hiatuses
950 in pelagic and hemipelagic strata. *Earth and Planetary Science Letters*, 224:55-72.

951 MCCANTA, M.C., HATFIELD, R.G., THOMAS, B.J., HOOK, S.J., and FISHER, E. *in review*.
952 Identifying cryptotephra units using correlated rapid, nondestructive methods: VSWIR
953 spectroscopy, X-ray fluorescence, and magnetic susceptibility. *Geochemistry Geophysics*
954 *Geosystems*.

955 MOLNAR, P., 2008. Closing of the Central American Seaway and the Ice Age: A critical review.
956 *Paleoceanography*, 23:PA2201.

957 OGG, J.G., 2012. The Geomagnetic Polarity Timescale. In: GRADSTEIN, F.M., OGG, J.G., and
958 SCHMITZ, M.D., Ogg, G.M, Eds., *The Geologic Time Scale 2012*, 85-113. Amsterdam: Elsevier.

959 OSBORNE, A.H., NEWKIRK, D.R., GROENVELD, J., MARTIN, E.E., TIEDEMANN, R., and
960 FRANK, M., 2014. The seawater neodymium and lead isotope record of the final stages of
961 Central American Seaway closure. *Paleoceanography*, 29:715-729. doi:10.1002/2014PA002676.

962 PÄLIKE, H., NORRIS, R.D., HERRLE, J.O., WILSON, P.A., COXALL, H.K., LEAR, C.H.,
963 SHACKLETON, N.J., TRIPATI, A.K., and WADE, B.S., 2006. The heartbeat of the Oligocene
964 climate system. *Science*, 314:1894-1898.

965 PALMER, M.R., HATTER, S.J., GERON, T.M., TAYLOR, R.N., CASSIDY, M., JOHNSON, P.,
966 LE FRIANT, A., and ISHIZUKA, O., 2016. Discovery of a large 2.4 Ma Plinian eruption of

967 Basse-Terre, Guadeloupe, from the marine sediment record. *Geology*, G37193.1.
968 doi:10.1130/G37193.1.

969 R CORE TEAM, 2014. R: A language and environment for statistical computing. *R Foundation for*
970 *Statistical Computing*, Vienna, Austria. URL <http://www.R-project.org/>.

971 REID, R.P., CAREY, S.N., and ROSS, D.R., 1996. Late Quaternary sedimentation in the Lesser
972 Antilles island arc. *GSA Bulletin*, 108:78-100.

973 THIERSTEIN, H.R., GEITZENAUER, K.R., MOLFINO, B., and SHACKLETON, N.J., 1977.
974 Global synchronicity of late Quaternary coccolith datum levels: Validation by oxygen
975 isotopes. *Geology*, 5:400-404.

976 TROFIMOV, J., FISHER, J.K., MACDONALD, H.A., TALLING, P.J., SPARKS, R.S.J., HART,
977 M.B., SMART, C.W., BOUDON, G., DEPLUS, C., and KOMOROWSKI, J.C., 2010. Evidence
978 for carbonate platform failure during rapid sea-level rise; ca 14,000 year old bioplastic flow
979 deposits in the Lesser Antilles. *Sedimentology*, 57:735-759.

980 WADE, B.S., PEARSON P.N., BERGGREN W.A., and PÄLIKE, H., 2011. Review and revision of
981 Cenozoic tropical planktonic foraminiferal biostratigraphy and calibration to the
982 geomagnetic polarity and astronomical time scale. *Earth-Science Reviews*, 104:111-142.

983 WALL-PALMER, D., COUSSENS, M., TALLING, P. J., JUTZELER, M., CASSIDY, M.,
984 MARCHANT, I., PALMER, M. R., WATT, S. F. L., SMART, C. W., FISHER, J. K., HART, M.
985 B., FRAASS, A. J., TROFIMOV, J., LE FRIANT, A., ISHIZUKA, O., ADACHI, T.,
986 ALJAHDALI, M., BOUDON, G., BREITKREUZ, C., ENDO, D., FUJINAWA, A., HATFIELD,
987 R., HORNBAACH, M. J., KATAOKA, K., LAFUERZA, S., MAENO, F., MANGA, M.,
988 MARTINEZ-COLON, M., MCCANTA, M., MORGAN, S., SAITO, T., SLAGLE, A. L.,

989 STINTO, A. J., SUBRAMANYAM, K. S. V., TAMURA, Y., VILLEMANT, B., and WANG, F.,
990 2014. Late Pleistocene stratigraphy of IODP Site U1396 and compiled chronology offshore of
991 south and south west Montserrat, Lesser Antilles. *Geochemistry, Geophysics, Geosystems*, 15.
992 doi: 10.1002/2014GC005402.

993 WEBB, S.D., 1997. The great American faunal interchange. In: COATES, A.G., Ed), *Central*
994 *America: A natural and cultural history*, 97-122. New Haven: Yale University Press.

995 ZHANG, X., PRANGE, M., STEPH, S., BUTZIN, M., KREBS, U., LUNT, D.J., NISANCIOGLU,
996 K.H., PARK, W., SCHMITTNER, A., SCHNEIDER, B., and SHULZ, M., 2012. Changes in
997 equatorial Pacific thermocline depth in response to Panamanian seaway closer: Insights
998 from a multi-model study. *Earth and Planetary Science Letters*, 317-318:76-84.

999

1000 **Figure Captions**

1001 Figure 1. Site Map. Map showing surface currents (black), as well as entry points for bottom
1002 waters (grey) to the Caribbean Sea. ODP Site 999 and IODP Site U1396 are highlighted as well.
1003 Base map from R-package 'maps' (Becker et al., 2015).

1004

1005 Figure 2. Stratigraphic data transformation process. First panel depicts major lithology for each
1006 hole (A, B, C) with Color Reflectance Brightness (L^*) for each hole (A is red, B green, and C
1007 blue). Key to the colors for the major lithology is shown on the far right. Depths for this panel
1008 are all on CCSF-A.

1009 Second panel depicts the spliced stratigraphy on the CCSF-A depth scale, with each hole
1010 as a distinct column. L^* in this panel only includes data included from the splice.

1011 Third panel depicts the composite section on the CCSF-D depth scale, with volcanic
1012 units and hemipelagic/pelagic sediments in distinct columns. L* in this panel is the spliced L*
1013 sequence.

1014 Fourth panel depicts the composite section removing all sediments with a volcanic
1015 major lithology. Both lithostratigraphic column and L* in this panel are not depicted as true
1016 depth, but are depicted on the CCSF-NV non-volcanic depth scale (See text).

1017

1018 Figure 3. Results of 0-1 Ma Evolutive Harmonic Analysis (EHA). Left-most panel is the L*
1019 brightness record, with volcanic sediments removed (CCSF-NV) and put on a paleomagnetic
1020 timescale. Second panel is the spectral power (hotter colors denote higher power). Third panel
1021 is amplitude of spectra (hotter colors denote larger amplitude at depicted frequency). Final
1022 panel is the results of the harmonic F-test, depicting where there is significant spectral power.
1023 The results of the harmonic F-test were used to tune. The horizontal black line on the final panel
1024 depicts a paleomagnetic sedimentation rate control point. White lines above and below depict
1025 the earliest that the EHA 'feels' the abrupt sedimentation rate change which occurs at the
1026 paleomagnetic datum. Note the 'smearing' about that point seen in the changing frequencies
1027 throughout the highlighted interval. Grey lines depict expected orbital frequencies (e
1028 eccentricity, o obliquity, p procession) if the sedimentation rate were constant. The green line
1029 depicts the frequency described by a 100-kyr period.

1030

1031 Figure 4. Summary of transformations from depth (CCSF-D) to Marine Isotope Ages for $\delta^{18}\text{O}$
1032 record. A is spliced core description lithostratigraphy, on the CCSF-D depth scale.

1033 Paleomagnetic stripe (B) is from Hatfield (2015; CCSF-D). Planktic foraminiferal biozonation (C)
1034 is from this study, CCSF-D. D separates the individual species $\delta^{18}\text{O}$ values (red is *Cibicidoides*
1035 *robertsonianus*, brown is *Cibicidoides mundulus*, black is *Planularia wuellerstofi*, orange is mixed)
1036 and plots them on the CCSF-D depth scale. PMag Age (E) is the species $\delta^{18}\text{O}$ records with ages
1037 as defined by a linear sedimentation rate from only paleomagnetic datums. Composite (F) is the
1038 composite $\delta^{18}\text{O}$ record on the Pmag Age scale (see 3. Methods). The light grey polygon behind
1039 the $\delta^{18}\text{O}$ values is the error associated with the $\delta^{18}\text{O}$ measurements (0.1‰ for *P. wuellerstofi*, and
1040 0.14‰ for other species, see 3. Methods). Astro Age (G) employs the astrochronology generated
1041 in this study for ages. LR04 Stack (H) is from Liesecki & Raymo (2005). MIS Age (I) is the
1042 isotopic data with a chronostratigraphy resulting from the correlations between the composite
1043 record (Astro Age, G) to the LR04 benthic stack (H). The LR04 stack then provides the
1044 numerical ages for the final age model (I). Individual grey lines of correlation cannot be traced
1045 across the entire figure, instead they were chosen to elucidate the individual transformations
1046 they connect. Lines from Astro Age (G) to LR04 Stack (H) to MIS Age (I) are continuous,
1047 however. Paleomagnetic stripe in J uses ages from Ogg et al. (2012). Within K, the first
1048 lithostratigraphic column is the hypothetical 'no volcanics' lithostratigraphic column (CCSF-
1049 NV) with age, while the second column is the true lithostratigraphic column with age. All colors
1050 follow Figure 2. All $\delta^{18}\text{O}$ scales are the same width.

1051
1052 Figure 5. Histogram of $\delta^{18}\text{O}$ offsets between benthic species. A depicts the offset between
1053 *Cibicidoides robertsonianus* and *Planulina wuellerstorfi*. Large black line depicts the combined
1054 machine errors for two measurements. Red line depicts the mean for the values within the

1055 histogram. Because there were only two samples with both species, the green line depicts the
1056 expected offset between *C. robertsonianus* to *P. wuellerstorfi* using *Cibicidoides mundulus* as an
1057 intermediary. B depicts the offset between *Cibicidoides mundulus* and *Planulina wuellerstorfi*.
1058 Large black line depicts the combined machine errors for two measurements. Red line depicts
1059 the mean for the values within the histogram. C depicts the offset between *Cibicidoides*
1060 *robertsonianus* and *Cibicidoides mundulus*. Large black line depicts the combined machine errors
1061 for two measurements. Red line depicts the mean for the values within the histogram.

1062

1063 Table 1. Table of planktic foraminifera biostratigraphic datums. Bolded lines denote datums
1064 used as primary zonal marker, unbolded lines denote secondary datums. Age columns are from
1065 Wade et al. (2011). a denotes an age calibrated to the Cande and Kent (1995) time scale, while b
1066 denotes calibration to the Lourens et al. (2004) astrochronological timescale. Sample is the
1067 highest or lowest sample in which the species was found. Sample Depths CSF-B uses the
1068 midpoint of the sample depths, and the shipboard composite depth scale. T [CCSF-D] and B
1069 [CCSF-D] is the possible range in depths for each datum. T PMag and B PMag is the range in
1070 age for each datum, derived from the linear paleomagnetic ages. T Astro and B Astro is the
1071 range in age for each datum, derived from the astrochronological tuning. T MIS and B MIS is
1072 the range in age for each datum, derived from the correlation to the LR04 benthic $\delta^{18}\text{O}$. Offset is
1073 the difference between the midpoint MIS age and the astrochronologically-tuned calibrated age
1074 (Wade et al., 2011). * denotes ages presented in Wall-Palmer et al. (2014). *Globorotalia flexuosa*
1075 was found in the first sample, while *Globorotalia crassaformis* s.l. was found in the last sample,
1076 and so neither datum has a true top or bottom, respectively.

1077
1078 Figure 6. Summary of differences between Wade et al. (2011) age datums and findings at Site
1079 U1396 with important Scanning Electron Micrographs (SEM). Ages for the biostratigraphic
1080 datums are presented as MIS ages, with the horizontal line corresponding to the
1081 chronostratigraphic position of the top or bottom. Primary datums are bolded. Colored datums
1082 correspond to the SEMs at the sides of the figure. Imaged foraminifera are either from the
1083 sample in which the datum was recorded (e.g., *Globorotalia pertenuis*) or nearby core catcher
1084 samples. Core catchers are not the precise base/top, as CC samples were not included in the
1085 splice. They are as close as was possible, however. All scale bars are 100 μm . *Globorotalia tumida*,
1086 *G. flexuosa* (aberrant form), and *G. flexuosa* are from Sample 340-U1396C-3H, CC. *Globorotalia*
1087 *pertenuis* is from Sample 340-U1396C-6H-3, 112-114 cm. *Dentoglobigerina altispira* is from Sample
1088 340-U1396C-8H, CC.

1089
1090 Figure 7. Summary of the two contrasting interpretations for the Brunhes chron
1091 chronostratigraphy. Left panel depicts the Wall-Palmer et al. (2014) interpretation, with this
1092 revised correlations only from MIS 15 to the base of the figure. Inset grey box is CARMON-2
1093 stratigraphy (Le Friant et al., 2008). Right panel depicts the proposed revision to the
1094 chronostratigraphy. %*Globorotalia menardii-tumida* zonation scheme (orange) is depicted as
1095 correlated to the marine isotope stages by Reid et al. (1996), which ends within zone T (approx.
1096 MIS 19). Black polygon is the % *G. menardii-tumida* from Wall-Palmer et al. (2014), while grey is
1097 the newly-generated data from this study (points denote samples counted). LR04 Stack (grey) is
1098 from Liseicki and Raymo (2005), planktic foraminiferal oxygen isotope stack (purple) is from

1099 Martinson et al. (1987). The *B. Emiliana huxleyi* datum within the left panel is the datum
1100 employed in Wall-Palmer et al. (2014), with the calibrated ages from Ogg et al. (2014), while the
1101 blue line (right panel only) refers to the other *B. E. huxleyi* (Aljahdali; unpublished Masters
1102 Thesis). Green line is the *Globigerinoides ruber* oxygen isotope record from Wall-Palmer et al.
1103 (2014), with new data beginning at approximately MIS 8 on the left panel, and MIS 13 on the
1104 right panel. Black rectangles are the paleomagnetic chron interpretation from Hatfield (2015).
1105 Sedimentation rates are calculated as m/myr. Stratigraphic columns follow figure 2. Slight
1106 offset in event bed from Wall-Palmer et al. (2014) and the lithostratigraphy presented here is
1107 due to the calculation of sediment ages and slight misfit in the correlated ages in this study. The
1108 event bed is the same as topmost volcanic unit.

1109
1110 Figure 8. Summary of the age vs. depth relationship of the Site U1396 sediments. Paleomagnetic
1111 datums are depicted in red squares, depths are from Hatfield (2015) while ages are from Ogg et
1112 al. (2012). Nannofossil datums are depicted in blue triangles, open for secondary and closed
1113 triangles for primary. Depths for nannofossil datums are from Expedition 340 Scientists (2013)
1114 unless noted as being from Wall-Palmer et al. (2014), ages are from Backman et al. (2012).
1115 Vertical blue line denotes uncertainty in true stratigraphic position of datum. Planktic
1116 foraminifera datums are depicted in green triangles, open for secondary and closed triangles for
1117 primary. Depths are from this study, ages are from the Wade et al. (2011) astrochronological
1118 calibration. Vertical line denotes uncertainty in true stratigraphic position of datum. Black
1119 diamond denotes a ^{14}C date (Accelerator Mass Spectrometry, AMS), and yellow diamond
1120 denotes MIS 5.5 and 6/7, identified within Wall-Palmer et al. (2014). Black line depicts a linear

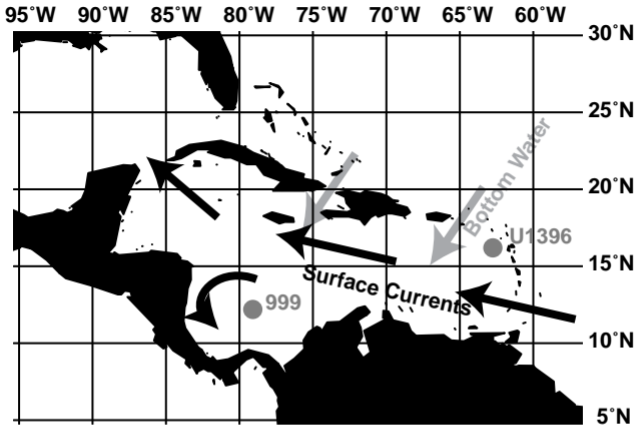
1121 interpolation for sediment age between paleomagnetic datums. The orange line depicts the ages
1122 from the astrochronological tuning. The brown line depicts the ages from the $\delta^{18}\text{O}$ correlation to
1123 the Marine Isotope Stages (MIS) within the LR04 benthic $\delta^{18}\text{O}$ stack (Liesecki and Raymo, 2005).

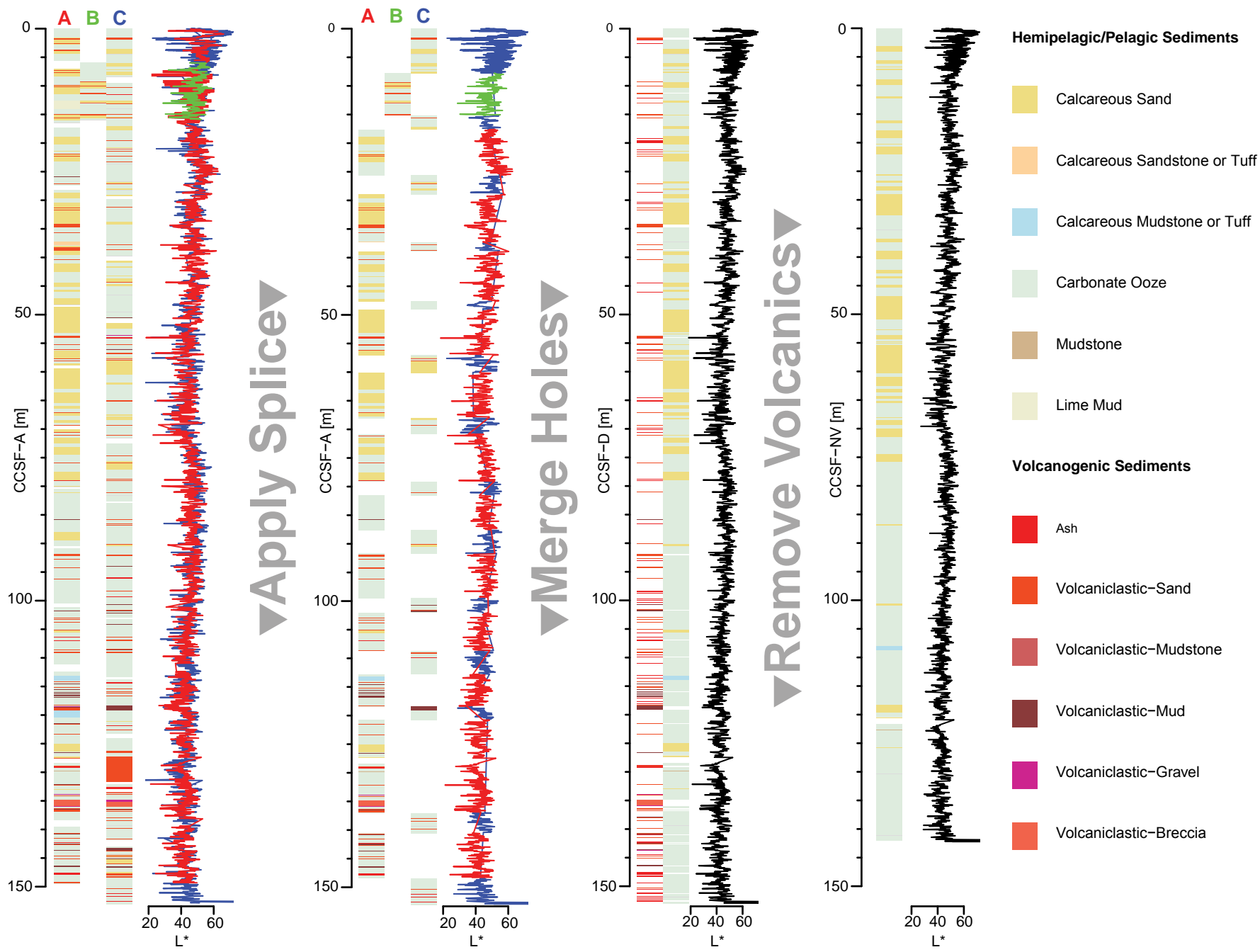
1124

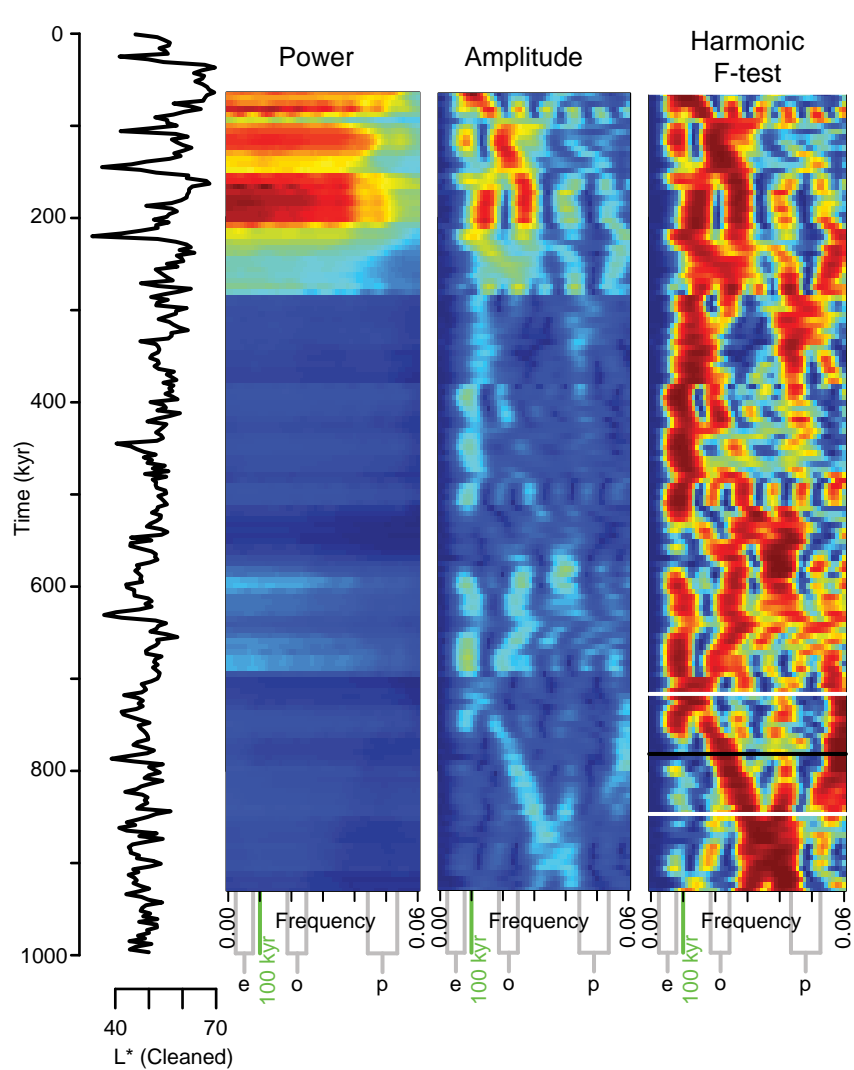
1125 Figure 9. Summary of differences in different methods of age calculation. Orange polygon
1126 represents the difference between the astrochronological ages and the paleomagnetic age for
1127 each sample included in the isotope record. Brown polygon represents the difference between
1128 the marine isotope stage (MIS) ages and the paleomagnetic age for each sample included in the
1129 isotope record. Red horizontal lines correspond to the ages of paleomagnetic reversals (Ogg et
1130 al., 2012).

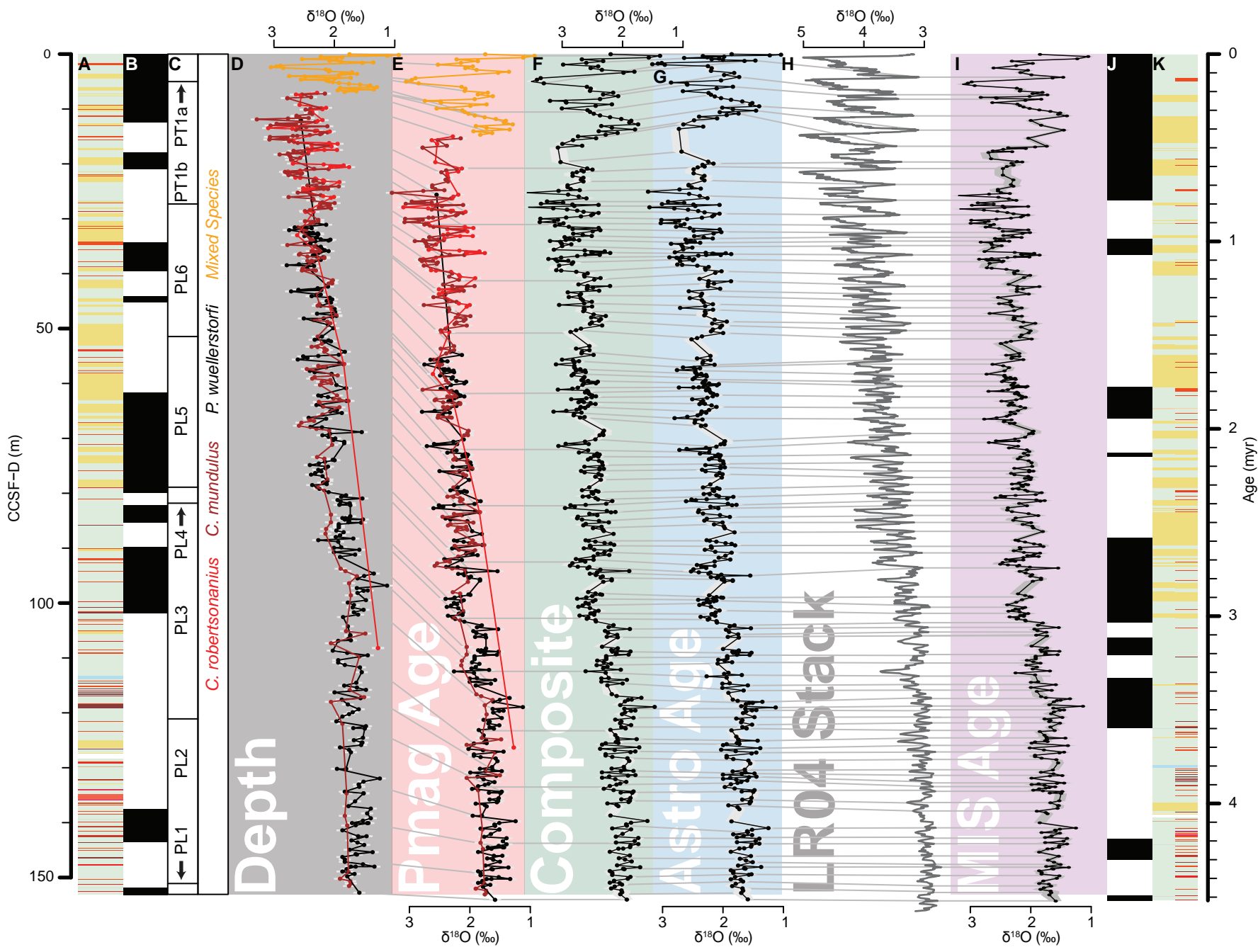
1131

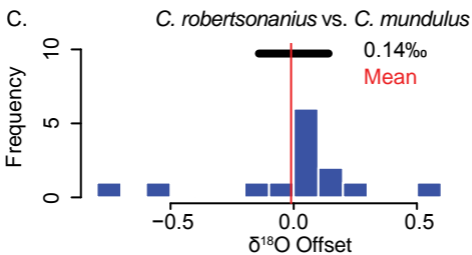
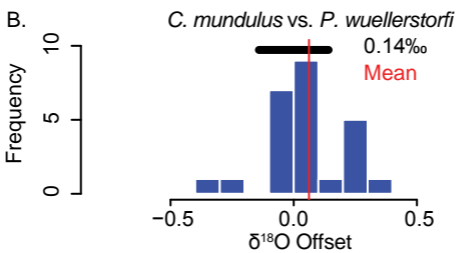
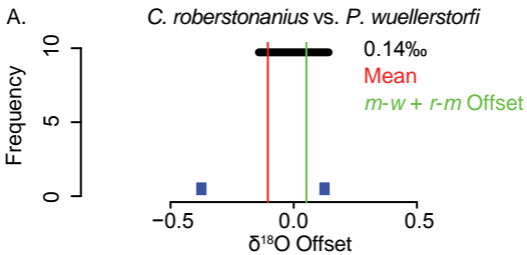
1132 Figure 10. Summary of sedimentation rates, paleoceanographic events, and sediment character.
1133 Upper panel depicts the L^* (brightness) parameter from shipboard measurements. Black line
1134 represents a 100-kyr running mean. Red dots are discrete $\text{CaCO}_3\%$ measurements from
1135 shipboard geochemistry. In the bottom panel, paleomagnetically derived sedimentation rates
1136 are in red (all sediment types), blue (no volcanic sediments), and purple (only volcanic
1137 sediments). MIS-age derived sedimentation rates are in orange (all sediment types) and green
1138 (no volcanic sediments). Inset depicts the correlation between L^* and MIS No Volc
1139 sedimentation rates. Blue boxes represent several pertinent paleoceanographic events while
1140 grey depict climatic events (see discussion for citations and numerical dates).



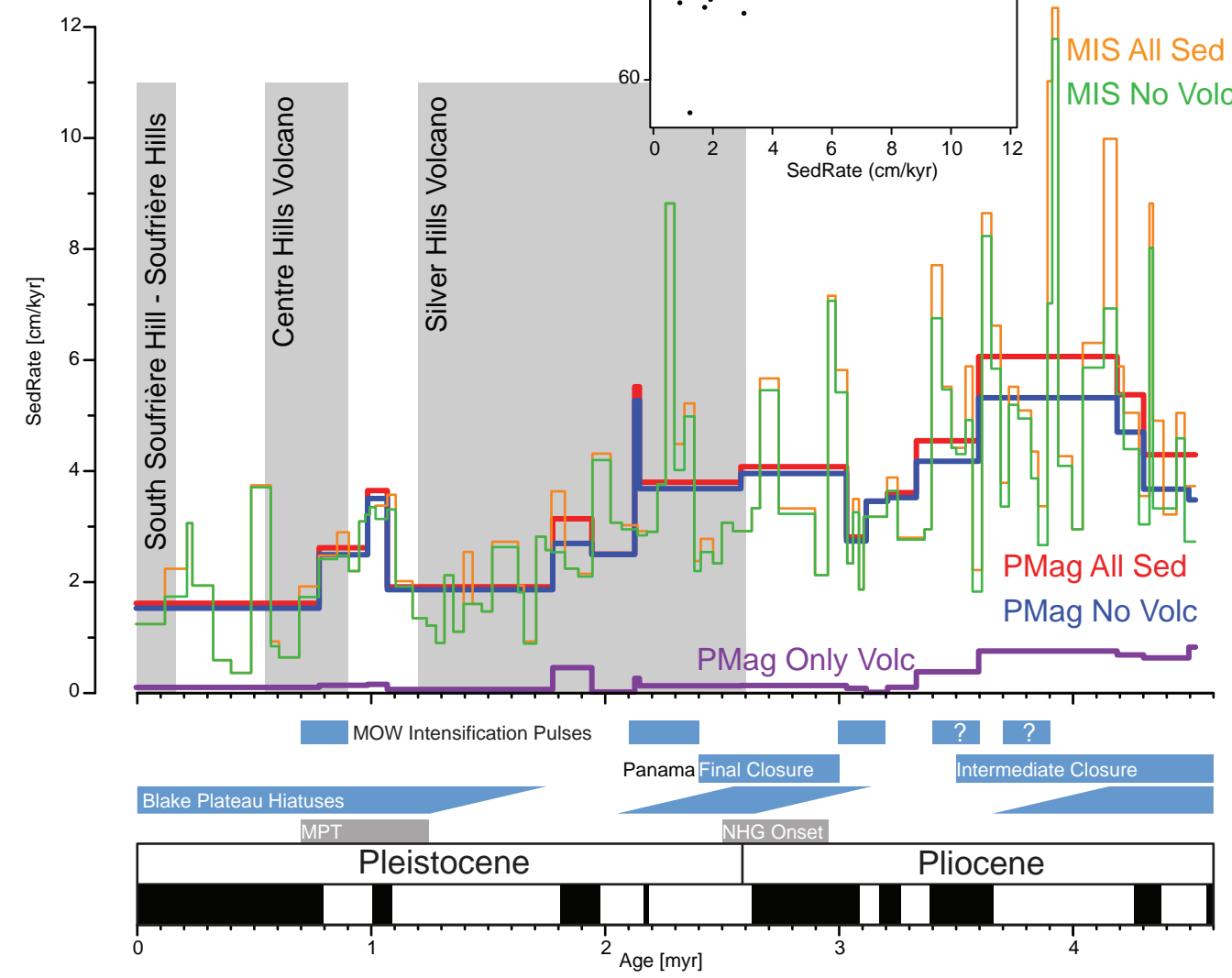
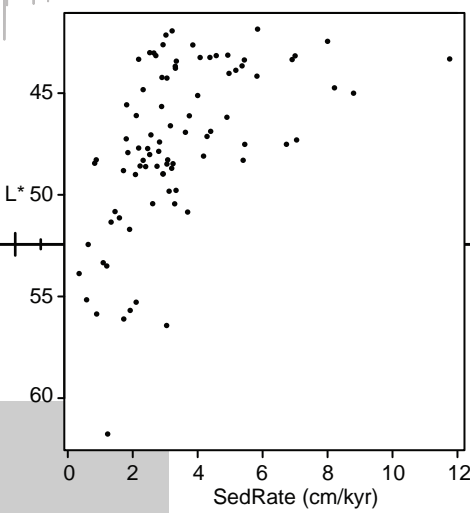
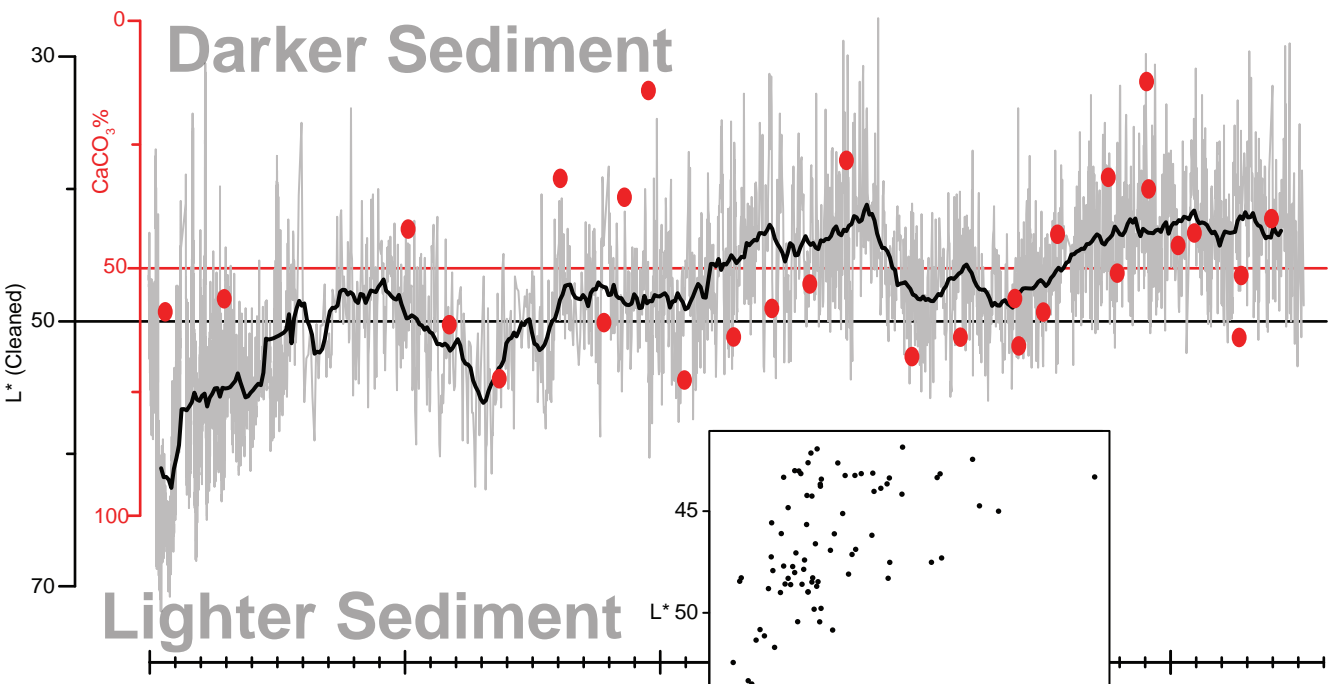




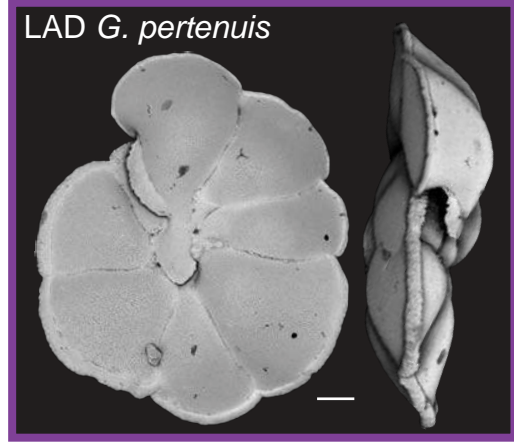
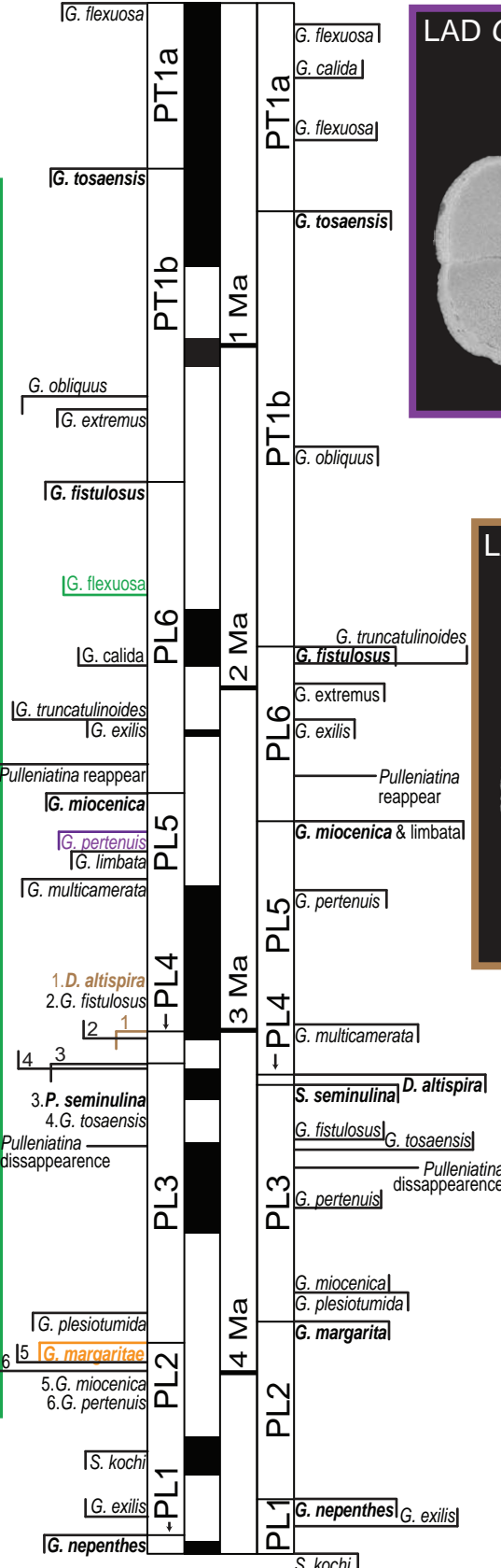




Species Datum	Age (Ma) ^a	Age (Ma) ^b	Sample	Sample Depth CSF-B	T [CCSF-D]	B [CCSF-D]	T PMag	B PMag	T Astro	B Astro	T MIS	B MIS	Offset
T <i>Globorotalia flexuosa</i>	0.07	0.07	U1396C/1H/1, 1-2cm	0.015	-	-	-	0.000	-	0.000	-	0.000	0.070
T <i>Globigerinella calida</i>	0.22	0.22	U1396C/4H/6, 125-127 cm	35.764	38.59	38.77	1.914	1.919	1.951	1.955	1.951	1.955	1.733
B <i>Globorotalia flexuosa</i>	0.40	0.40	U1396C/4H/3, 47-49 cm	30.723	33.31	33.33	1.724	1.724	1.742	1.742	1.754	1.754	1.354
B <i>Globorotalia hirsuta</i>	0.45	0.45	<i>Not present at Site</i>										
T <i>Globorotalia tosaensis</i>	0.61	0.61	U1396C/1H/5, 90-91 cm	6.905	-	-					0.494*	0.495*	0.116
B <i>Globorotalia hessi</i>	0.75	0.75	<i>Not present at Site</i>										
B <i>Globorotalia excelsa</i>	1.00	1.00	<i>Not present at Site</i>										
T <i>Globoturborotalita obliquus</i>	1.30	1.30	U1396C/3H/3, 21-23 cm	20.953	22.01	22.51	1.129	1.154	1.106	1.124	1.116	1.140	0.172
T <i>Goides fistulosus</i>	1.88	1.88	U1396C/3H/6, 51-53 cm	25.504	27.13	27.31	1.398	1.407	1.428	1.438	1.436	1.456	0.434
B <i>Globorotalia truncatulinoides</i>	1.93	1.93	U1396C/5H/2, 110-112 cm	39.353	43.21	43.81	2.092	2.116	2.113	2.126	2.073	2.092	0.152
T <i>Globigerinoides extremus</i>	1.99	1.98	U1396C/3H/3, 85-87 cm	21.560	22.97	23.15	1.179	1.188	1.144	1.152	1.164	1.172	0.812
B <i>Pulleniatina finails</i>	2.05	2.04	<i>Pulleniatina not split</i>										
T <i>Globorotalia exilis</i>	2.10	2.09	U1396C/5H/2, 110-112 cm	39.353	42.96	43.23	2.082	2.092	2.108	2.113	2.064	2.073	0.022
Reappearance of <i>Pulleniatina</i>	2.26	2.26	U1396C/5H/6, 3-5 cm	43.986	48.16	48.43	2.226	2.233	2.219	2.228	2.237	2.244	0.019
T <i>Globoturborotalita woodi</i>	2.30	2.30	<i>Not present at Site</i>										
T <i>Globorotalia pertenuis</i>	2.60	2.60	U1396C/6H/3, 112-114 cm	50.312	55.33	55.64	2.416	2.424	2.382	2.387	2.362	2.367	0.236
T <i>Globorotalia miocenica</i>	2.39	2.39	U1396A/6H/2, 125-127 cm	46.178	49.91	51.46	2.273	2.313	2.261	2.297	2.270	2.288	0.111
T <i>Globorotalia limbata</i>	2.39	2.39	U1396C/6H/5, 20-22 cm	52.282	57.36	57.72	2.470	2.479	2.435	2.445	2.421	2.433	0.037
T <i>Globoturborotalita decoraperta</i>	2.75	2.75	<i>Not present at Site</i>										
T <i>Globorotalia multicamerata</i>	2.99	2.98	U1396C/6H/7, 34-36 cm	55.257	60.26	60.86	2.546	2.562	2.532	2.553	2.529	2.548	0.442
T <i>Dentoglobigerina altispira</i>	3.13	3.13	U1396C/8H/5, 27-29 cm	71.335	78.49	78.91	2.998	3.007	3.004	3.014	3.003	3.010	0.124
T <i>Sphaeroidinellopsis seminulina</i>	3.16	3.16	U1396C/8H/7, 14-16 cm	74.080	81.51	81.82	3.090	3.101	3.085	3.098	3.077	3.085	0.079
B <i>Globigerinoides fistulosus</i>	3.33	3.33	U1396C/8H/5, 115-117 cm	72.165	79.77	80.37	3.029	3.049	3.035	3.049	3.025	3.035	0.300
B <i>Globorotalia tosaensis</i>	3.35	3.35	U1396A/9H/2, 19-21 cm	73.741	82.17	82.19	3.114	3.114	3.115	3.115	3.105	3.105	0.245
Disappearance of <i>Pulleniatina</i>	3.41	3.41	U1396C/9H/5, 124-126 cm	81.801	89.93	90.27	3.333	3.340	3.361	3.370	3.570	3.365	0.058
B <i>Globorotalia pertenuis</i>	3.51	3.52	U1396C/13H/2, 30-32 cm	114.688	125.84	125.86	3.993	3.993	4.000	4.000	4.025	4.025	0.505
T <i>Pulleniatina primalis</i>	3.65	3.65	<i>Pulleniatina not split</i>										
B <i>Globorotalia miocenica</i>	3.76	3.77	U1396C/13H/1, 48-50 cm	113.384	124.52	124.54	3.971	3.971	3.971	3.971	3.985	3.985	0.215
T <i>Globorotalia plesiotumida</i>	3.76	3.77	U1396A/12H/3, 38-40 cm	103.950	115.79	115.88	3.827	3.828	3.841	3.842	3.850	3.852	0.081
T <i>Globorotalia margaritae</i>	3.84	3.85	U1396C/12H/5, 135-137 cm	110.696	89.85	89.83	3.331	3.341	3.359	3.370	3.355	3.365	0.490
B <i>Globorotalia crassaformis</i> s.l.	4.30	4.31	<i>Present in last sample</i>	139.110	152.75	152.77	4.514	-	4.513	-	4.520	-	
T <i>Globoturborotalita nepenthes</i>	4.36	4.37	U1396C/15H/6, 62-64 cm	137.540	150.64	151.10	4.465	4.475	4.454	4.466	4.466	4.475	0.101
B <i>Globorotalia exilis</i>	4.44	4.45	U1396C/15H/4, 139-141 cm	135.473	148.88	148.99	4.424	4.426	4.405	4.408	4.426	4.429	0.022
B <i>Sphaeroidinellopsis kochi</i>	4.52	4.53	U1396C/14H/6, 60-62 cm	128.202	140.06	140.08	4.234	4.234	4.232	4.232	4.232	4.232	0.298

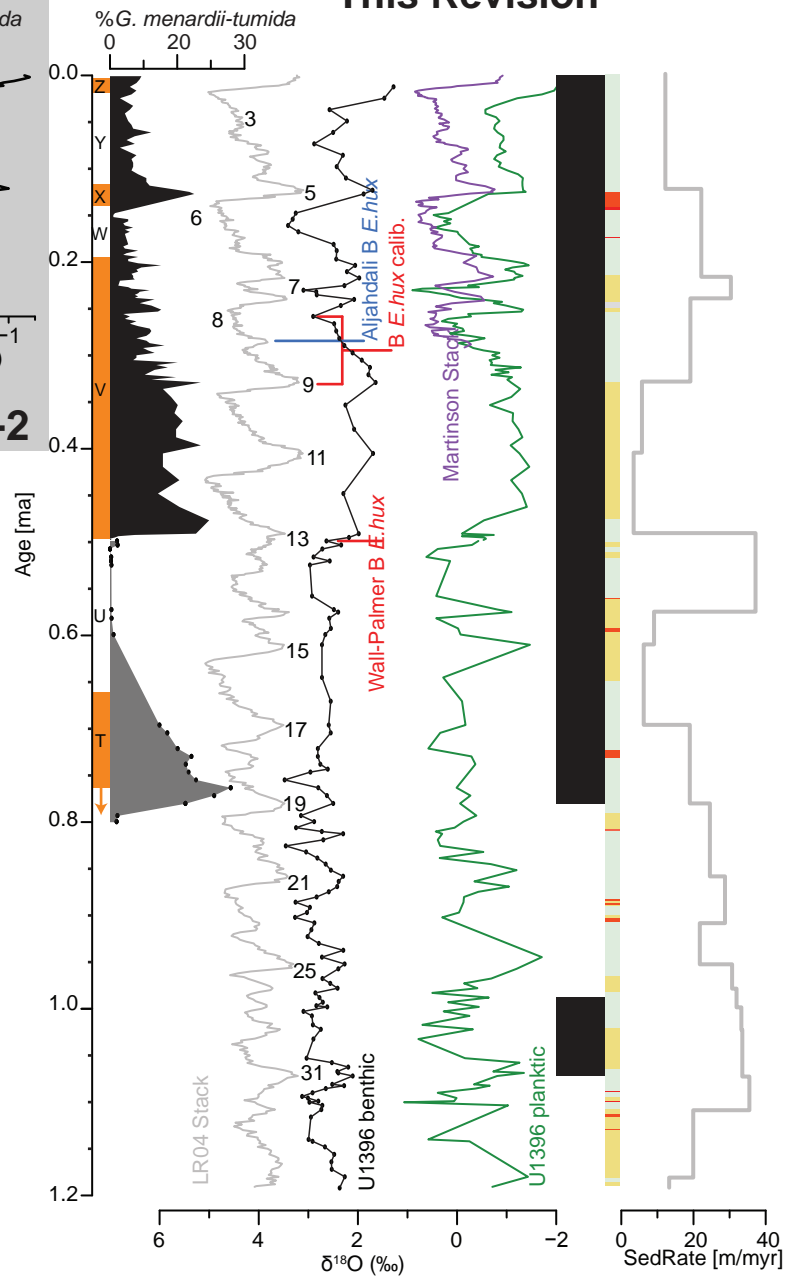
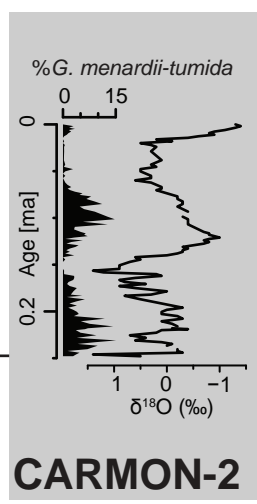
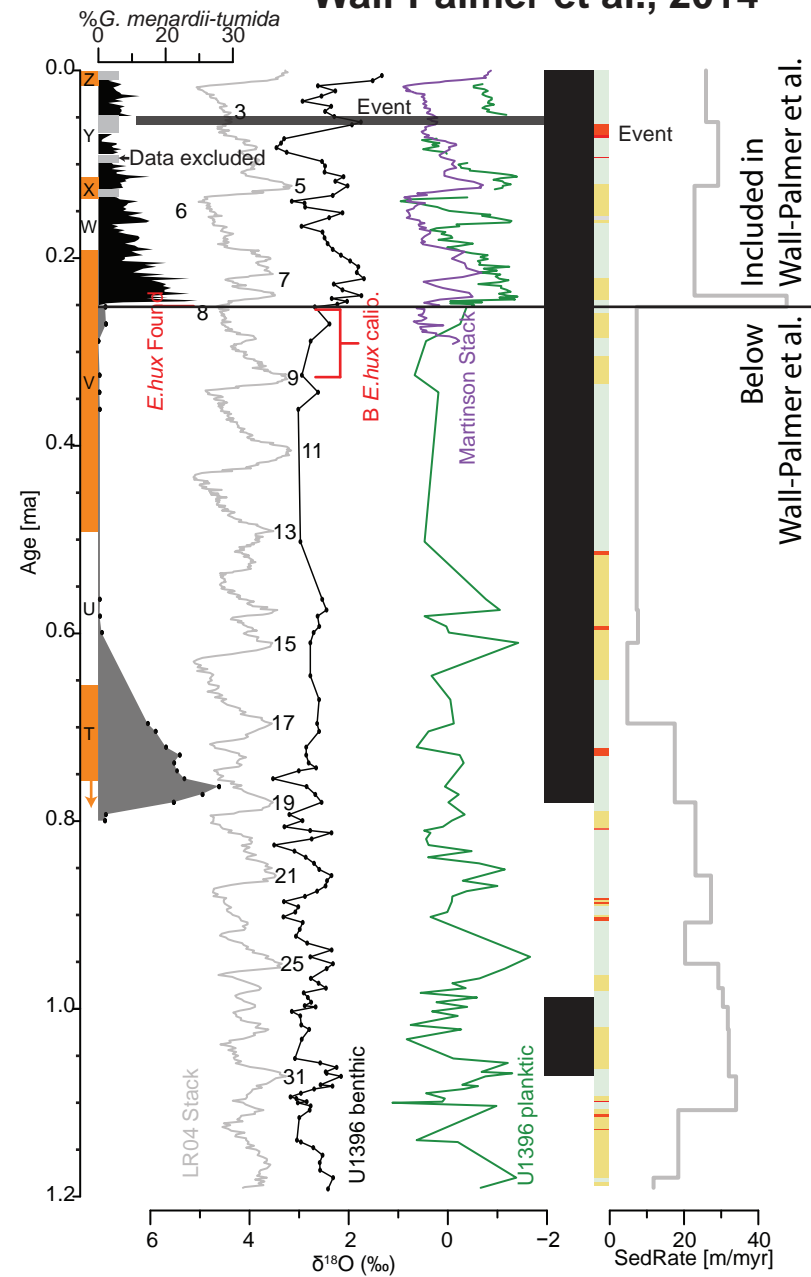


Top
Secondary Primary
Bottom

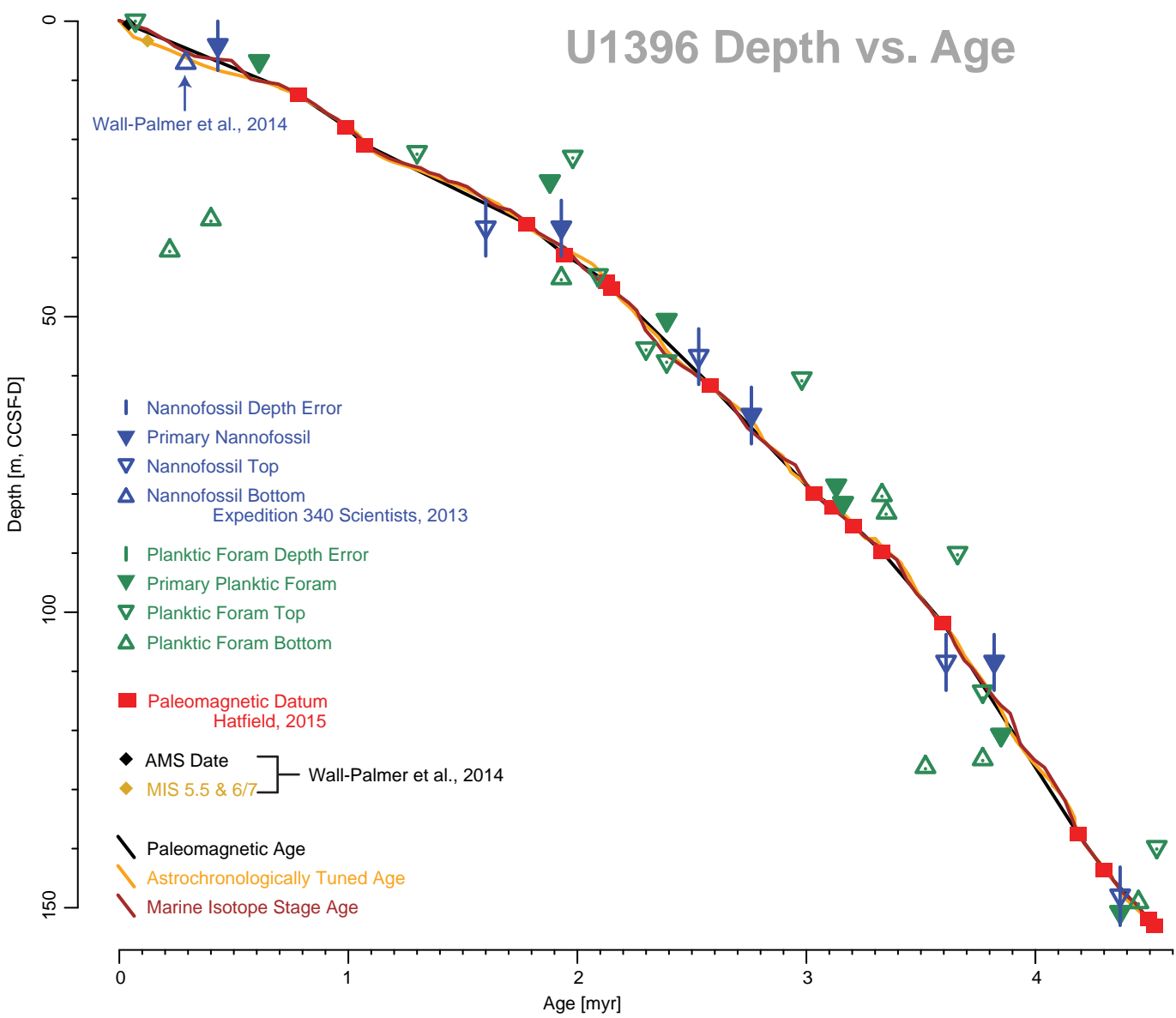


Wall-Palmer et al., 2014

This Revision



U1396 Depth vs. Age



Older than Linear Pmag

Younger

